Journal of Applied Fluid Mechanics, Vol. 18, No. 11, pp. 2852-2873, 2025.
Available online at www.jafmonline.net, ISSN 1735-3572, EISSN 1735-3645.
https://doi.org/10.47176/jafm.18.11.3362

Multi-objective Optimization of Single-stage High-flow Centrifugal Blower Based on Sparrow Search Algorithm-back Propagation Neural Network and Non-dominated Sorting Genetic Algorithm - Ⅱ

C. Lei[1], J. Zhang[2], F. Li[3], Z. Wang[1], H. Yang[1], W. Zhang[1] and Y. Wei[†1,3]

[1] *Zhejiang Key Laboratory of Multiflow and Fluid Machinery,Zhejiang Sci-Tech University, Hangzhou, Zhejiang 310018, China*
[2] *Denair Energy Equipment Co., Ltd., Jiaxing, Zhejiang 314211, China*
[3] *General Machinery and Key Basic Component Innovation Center (Anhui) Co., Ltd, State Key Laboratory of High-end Compressor and System Technology, Hefei General Machinery Research Institute Co., Ltd., Hefei, Anhui 230031, China*

†*Corresponding Author Email:yikunwei@zstu.edu.cn*

ABSTRACT

In this paper, the aerodynamic performance of the single-stage high-flow centrifugal blower is enhanced and optimized through multi-objective optimization by modifying the geometry parameters of the impeller. Seven design variables, which define the angle distribution of the impeller, are employed to parameterize its geometry. The polytropic efficiency and total pressure ratio of the centrifugal blower are selected as the two primary objective functions in the optimization process. The geometric parameters of the centrifugal impeller are sampled using the Latin Hypercube Sampling (LHS) method. Based on Computational Fluid Dynamics (CFD), the sample library comprising 60 sets of new geometric parameters for centrifugal impellers. The Sparrow Search Algorithm-Back Propagation Neural Network (SSA-BPNN) is utilized to train the sample set. Subsequently, the second-generation Non-dominated Sorting Genetic Algorithm (NSGA-II) is employed for the optimization of the centrifugal blower. Compared with the reference centrifugal impeller, the optimized impeller demonstrates a higher average outlet relative Mach number and a lower absolute Mach number at the outlet, leading to improved flow uniformity at the impeller exit. The flow separation on the diffuser blades is diminished, and the vortex structure near the impeller shroud is reduced. The polytropic efficiency and total pressure ratio of the centrifugal blower increase by up to 2.49% and 3.18%, respectively. The operational range with high polytropic efficiency is effectively expanded for the centrifugal blowers. The aforementioned findings underscore the effectiveness of the deployed multi-objective optimization techniques in refining the performance of the centrifugal blower.

Article History

Received January 27, 2025
Revised May 27, 2025
Accepted June 18, 2025
Available online September 3, 2025

Keywords:

Single-stage centrifugal blower
Multi-objective optimization
Sparrow Search Algorithm-Back Propagation Neural Network
Non-dominated Sorting Genetic Algorithm - Ⅱ
Computational fluid dynamics

1. INTRODUCTION

Centrifugal compressors are extensively utilized and hold significant importance in various industrial settings, including power plants and wastewater treatment plants. To ensure optimal performance, it is crucial to maximize the efficiency and pressure ratio of the compressor. In the practical engineering optimization process of centrifugal compressors, many complex problems are faced, e.g., multimodal and highly nonlinear design space (Arias-Montaño et al., 2011; Nejat et al., 2014).

In general, numerical optimization technique is an effective tool to improve the efficiency of centrifugal compressor. Meanwhile, contemporary optimization algorithms, such as genetic algorithms (GAs), have been improved to effectively address these issues and have demonstrated the ability to comprehensively explore the solution space and determine global optimal solutions with high probability. Modern optimizers include genetic algorithms (Holland, 1975), simulated annealing (Kirkpatrick et al., 1983), particle swarm optimization (Kennedy & Eberhart, 1995), ant colony optimization (Colorni et al., 1992),and etc. The entire solution space and global optima were explored, local optima from initial values had efficiently reached (Li et al., 2019), the computational burden of optimization was significantly reduced.

The precise aerodynamic performance of the centrifugal compressor is achieved through precise numerical simulation. Additionally, optimizers need to assess a large number of samples for function evaluation (Zhang et al., 2016), resulting in high computational cost, time consumption, and inefficiency in the connection between modern optimizers and three-dimensional numerical simulators (Ou et al., 2019). Therefore, to reduce the computational cost, an approximate modelling approach is used in the design space of centrifugal blower. It is necessary to significantly reduce the computational cost but provide an approximation of the design space. Researchers have used many techniques for approximate modelling such as Kriging (Tang et al., 2021), Response Surface Modelling (Roy et al., 2020), Artificial Neural Networks (Mengistu & Ghaly, 2008; Wang et al., 2022), Support Vector Regression (SVR) (Ju et al., 2016) etc. Neural networks have strong capabilities for global modeling, high accuracy, flexibility, and are widely used in various engineering and research fields. High-accuracy modeling requires a high-quality database (Verstraete et al., 2010), and the selection of samples significantly impacts the richness of information within the database. Therefore, there is a need to construct rich databases with minimal samples to minimize costs. While random sampling methods are commonly used due to their simplicity (Ekradi & Madadi, 2020). To ensure that any set of samples is representative of the entire sample space, it is essential to choose an appropriate sampling method. Latin hypercube sampling (Wei et al., 2020) guarantees inclusion of the entire design variable space and non-random distribution of samples while maintaining control over their logic.

Chen et al. (2023) integrated the empirical one-dimensional loss model, statistical analysis methods, and multi-optimization theories to initiate the preliminary design of one - dimensional parameters. They employed a multi - objective optimization strategy based on the grey relational grade (GRG) to explore the optimal combination of one - dimensional parameters. Through this process, they successfully reduced power consumption and enhanced the isentropic efficiency. Wang et al. (2024) utilized the NSGA - II multi - objective optimization algorithm to seek solutions for the electric turbo compressor (ETC) that could simultaneously meet the requirements of low axial thrust and low power consumption. Sun et al. (2024b) dedicated efforts to developing and calibrating the computational fluid dynamics (CFD) simulation model and the Stacking model. On this solid foundation, a novel multi - objective random walk grey wolf optimization algorithm (MORW - GWO) was proposed to conduct multi - objective optimization on the structural parameters of the compressor. After optimization, significant improvements were achieved in several key performance indicators, such as adiabatic compression work, pressure ratio, and isentropic efficiency. Fu et al. (2024) conducted an in - depth study on the prediction performance of the linear - based Boosting model and carried out multi - objective optimization on the impeller structural parameters by means of the reference vector guided evolutionary algorithm (RVEA). Through this optimization process, the isentropic efficiency and pressure ratio not only were increased, but also the shock wave loss of the gas was significantly reduced, the entropy increase was decreased, and the flow stability was further enhanced. How do we restrain the separate flow of the impeller to improve the isentropic efficiency of the centrifugal blower and broaden the efficient zone of the centrifugal blower based on SSA-BPNN and NSGA-II. This is also the dream of the centrifugal blower designers to achieve energy-saving goals with minimal cost.

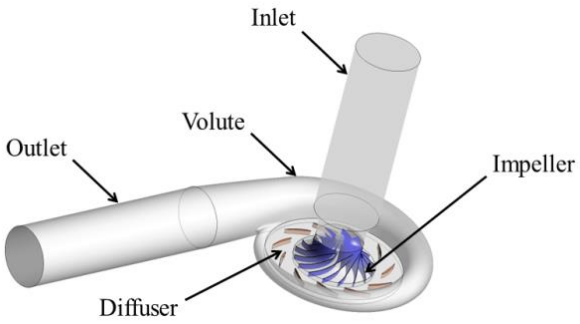

Fig. 1 Computation domain of the centrifugal blower

Based on the aforementioned discussion, this paper mainly focuses on identifying the optimal centrifugal impeller geometry to improve the efficiency and pressure ratio of a single-stage, centrifugal blower in this paper. A novel approach, termed SSA-BPNN, is discussed and employed to construct the surrogate model. Predictive models from impeller geometric parameters to centrifugal blower performance are developed through SSA-BPNN. Additionally, the NSGA-II is utilized for multi-objective optimization. Numerical results of the baseline and optimum blowers are qualitatively and quantitatively compared using CFD. This paper is structured as follows. In section 2, a concise description of governing equations and numerical methods is provided. In section 3, on the optimization process, the optimization algorithm and final optimization blade model are elaborated. Subsequently, the detailed discussions of numerical results are presented. Finally, some conclusions are provided.

2 GOVERNING EQUATIONS AND NUMERICAL METHOD

2.1 Model of Baseline Centrifugal Blower

Figure 1 depicts the overall computational scope of the centrifugal blower. The centrifugal blower mainly consists of a semi-open impeller with three-dimensional blades, a diffuser with airfoil blades and volute. By extending the centrifugal impeller inlet and the volute outlet, a complete range of calculations is established. The components of the centrifugal blower are labeled as shown in Fig. 1.

The shaft speed of the centrifugal blower is 21000rpm and the design mass flow rate is equal to 5.4kg/s. In addition, the geometry parameters of baseline impeller are listed in Table 1.

Table 1 Main parameters of the centrifugal blower and baseline impeller

Parameters	Values (Unit)
Shaft speed	21000(rpm)
Design mass flow rate	5.4(kg/s)
Blade counts full/splitter	8/8(-)
Unshroud tip clearance(in/out)	0.8/0.8(mm)
Inlet blade height	89.6(mm)
Inlet tip diameter	221(mm)
Hub diameter	44(mm)
Meridional depth of Impeller outlet (b2)	22(mm)
Exit diameter	370(mm)
Blade angle of backswept angle	46(degree)

2.2 Governing Equations of Fluid Flow

Three-dimensional governing equation for compressible fluid is applied in the fluid analyses conducted of the blower. (Menter, 1994; Yang et al., 2019; Wang et al., 2020). The mathematical formulations of these equations are presented.

The continuity equation is

$$\frac{\partial \rho}{\partial t}+\frac{1}{r}\left[\frac{\partial\left(\rho v_r r\right)}{\partial r}+\frac{\partial\left(\rho v_0\right)}{\partial \theta}+\frac{\partial\left(\rho v_z r\right)}{\partial z}\right]=0 \tag{1}$$

The momentum equation is

$$\begin{aligned}\rho\left(\frac{dv_r}{dt}-\frac{v_\theta^2}{r}\right)&=\rho F_{br}+\frac{1}{r}\frac{\partial\left(p_{rr}r\right)}{\partial r}+\frac{1}{r}\frac{\partial\left(p_{r\theta}\right)}{\partial \theta}\\&+\frac{1}{r}\frac{\partial\left(p_{rz}r\right)}{\partial z}-\frac{1}{r}p_{\theta\theta}\end{aligned} \tag{2}$$

$$\begin{aligned}\rho\left(\frac{dv_\theta}{dt}-\frac{v_r v_\theta}{r}\right)&=\rho F_{b\theta}+\frac{1}{r}\frac{\partial\left(p_{rr}r\right)}{\partial r}+\frac{1}{r}\frac{\partial\left(p_{r\theta}\right)}{\partial \theta}\\&+\frac{1}{r}\frac{\partial\left(p_{rz}r\right)}{\partial z}+\frac{1}{r}p_{r\theta}\end{aligned} \tag{3}$$

$$\begin{aligned}\rho\frac{dv_z}{dt}&=\rho F_{bz}+\frac{1}{r}\frac{\partial\left(p_{rz}r\right)}{\partial r}\\&+\frac{1}{r}\frac{\partial\left(p_{\theta z}\right)}{\partial \theta}+\frac{1}{r}\frac{\partial\left(p_{zz}r\right)}{\partial z}\end{aligned} \tag{4}$$

where ρ is the density, and v_r , v_θ and v_z are velocity components at different directions of cylindrical coordinate system, respectively.

The total energy equation is

$$\begin{aligned}\rho\frac{dH}{dt}&=\frac{1}{r}\frac{\partial}{\partial r}\left(rk\frac{\partial T}{\partial r}\right)+\frac{1}{r}\frac{\partial}{\partial \theta}\left(\frac{k}{r}\frac{\partial T}{\partial \theta}\right)\\&+\frac{1}{r}\frac{\partial}{\partial z}\left(rk\frac{\partial T}{\partial z}\right)+\rho q+\frac{dp}{dt}+\varphi\end{aligned} \tag{5}$$

where k is the heat transfer coefficient of the fluid medium.

2.3 Turbulence Model

The turbulence model used in this study for numerical calculations of centrifugal blowers is shear stress transport (SST). The SST model employs a blending function that utilizes the $k-\omega$ model in proximity to the wall and switches to the $k-\varepsilon$ model in regions away from the boundary layer (Li et al., 2012; Xue & Shen, 2020), fully leveraging the advantages of both. Consequently, the SST model is capable of accurately reproducing minor fluctuations in the fluid adjacent to the wall, while simultaneously preventing the phenomenon of excessive sensitivity to the incoming flows. This model has demonstrated improved prediction accuracy in calculations. (Ju et al., 2016) Due to these advantages, the SST turbulence model is widely employed in compressor flow studies (Ju et al., 2021). The governing equations of the SST turbulence model are

$$v_t=\frac{\alpha_1 k}{\max(\alpha_1\omega, SF_2)} \tag{6}$$

$$\begin{aligned}\frac{\partial k}{\partial t}+\frac{\partial(ku_i)}{\partial x_i}&=\frac{\partial}{\partial x_j}\left[\left(v+\frac{v_t}{\sigma_k}\right)\frac{\partial k}{\partial x_j}\right]\\&+G_k-k\omega\beta^*\end{aligned} \tag{7}$$

$$\begin{aligned}\frac{\partial \omega}{\partial t}+\frac{\partial(\omega u_i)}{\partial x_i}&=\frac{\partial}{\partial x_j}\left[\left(v+\frac{v_t}{\sigma_\omega}\right)\frac{\partial \omega}{\partial x_j}\right]\\&+\frac{\alpha\omega}{k}G_k-\omega\beta^2\\&+2\left(1-F_1\right)\frac{1}{\omega\sigma_\omega}\frac{\partial k}{\partial x_j}\frac{\partial \omega}{\partial x_j}\end{aligned} \tag{8}$$

where v_t represents the turbulent viscosity, k is the turbulent kinetic energy, α_1 is the model constant, ω represents the turbulence frequency, S is the estimated strain rate, v denotes the kinematic viscosity coefficient, F_1 and F_2 are different mixing functions, and G_k denotes the turbulence kinetic energy generation term caused by the velocity gradient, respectively.

2.4 Simulation Settings

In this paper, numerical simulations are performed using the ANSYS CFX2023R2 software. The turbulence model used for the numerical simulations is the SST model. The fluid medium is ideal air, and 0 atm is designated as the ambient reference pressure. The simulation incorporates a smooth wall and non-sliding boundary with the heat transfer set to adiabatic. The rotation speed of the centrifugal blower is 21000 rpm, and the total pressure and total temperature are specified as 101.325 kPa and 293.15 K at the inlet boundary, respectively. The mass flow rate is selected at the outlet boundary condition. Numerical simulations of the centrifugal blower are conducted at various mass flow rates. The internal flow characteristics between the baseline blower and the optimum blower are also analyzed at actual working flow rates.

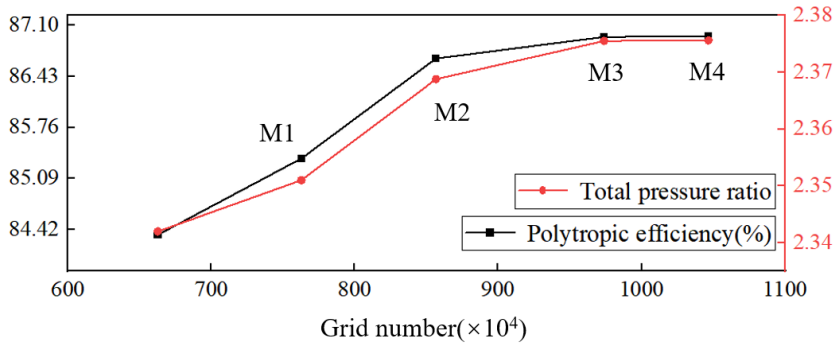

Fig. 2 Total pressure ratio and polytropic efficiency for different numbers of nodes

Table 2 Mesh dependency study of centrifugal impellers

	M1	M2	M3	M4
Nodes (×10^4)	362.8	411.5	473.9	546.7
Polytropic Efficiency	85.352	86.6613	86.9478	86.9621
Difference (%)	—	1.5222	1.86967	0.18864
Total Pressure Ratio	2.351	2.3688	2.3755	2.3746
Difference (%)	—	0.757125	1.04211	1.003828

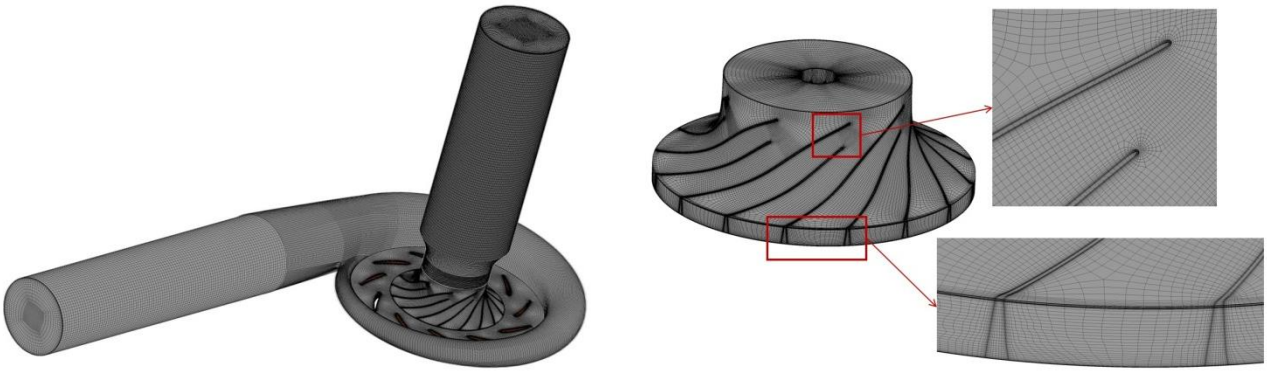

(a) (b)

Fig. 3 Computation domain mesh of centrifugal blowers (a) whole computation domain and (b) impeller

2.5 Grid System and Independence

Figure 2 depicts the mesh structure of the centrifugal blower. The hexahedral structure mesh of the entire computation domain is shown in Fig. 2(a). The centrifugal impeller is of critical importance in the acceleration of airflow, functioning as the indispensable component of a high-performance blower. It is essential to utilize a high-quality mesh discretization in order to achieve accurate numerical simulation of complex three-dimensional blades. Figure 2(b) offers a comprehensive illustration of the impeller mesh with particular attention to the intricate mesh near the leading edge (LE) and trailing edge (TE) of the blade.

The mesh dependency of the centrifugal impeller is performed to obtain the best grid for the study. Numerical results are tabulated in Table 2. The M1, M2, M3 and M4 are represented at different grids, and the resolution of the grid gradually increases from M1 to M4. As shown in Table 1, there is no noticeable variance in the actual operating point efficiency between mesh M3 and M4. Figure 2, which illustrates the variation of polytropic efficiency and total pressure ratio across different mesh densities for the entire computational domain of the centrifugal blower. When the impeller mesh count is set to M3, the total mesh count for the entire computational domain is 9.739 million. Increasing the impeller mesh density to M4 resulted in a total mesh count of 10.467 million. At this point, the deviations in the total pressure ratio and polytropic efficiency were negligible. Therefore, we selected the grid with a total mesh count of 9.739 million (including 4.739 million for the impeller domain) for subsequent numerical simulations, as it provided a balance between computational accuracy and efficiency.

Figure 3 shows the computational domain mesh of the centrifugal blower. In this study, a multi-block structural mesh with hexahedral elements is generated based on the M3 mesh and the detailed meshing of the blades of the centrifugal blower impeller is presented at the leading and trailing edges. All numerical calculations, including database creation and optimization, are carried out using this specific mesh configuration.

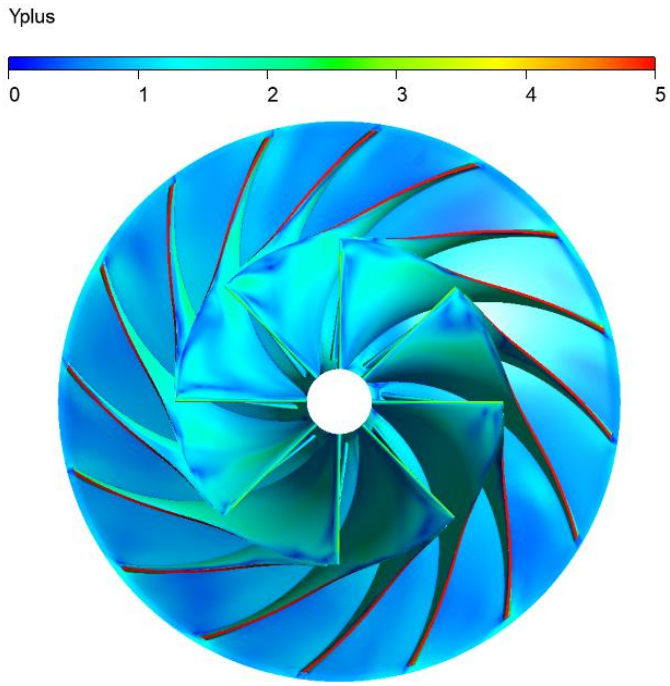

Fig. 4 Y plus distribution at the centrifugal impeller blade and hub of the blower

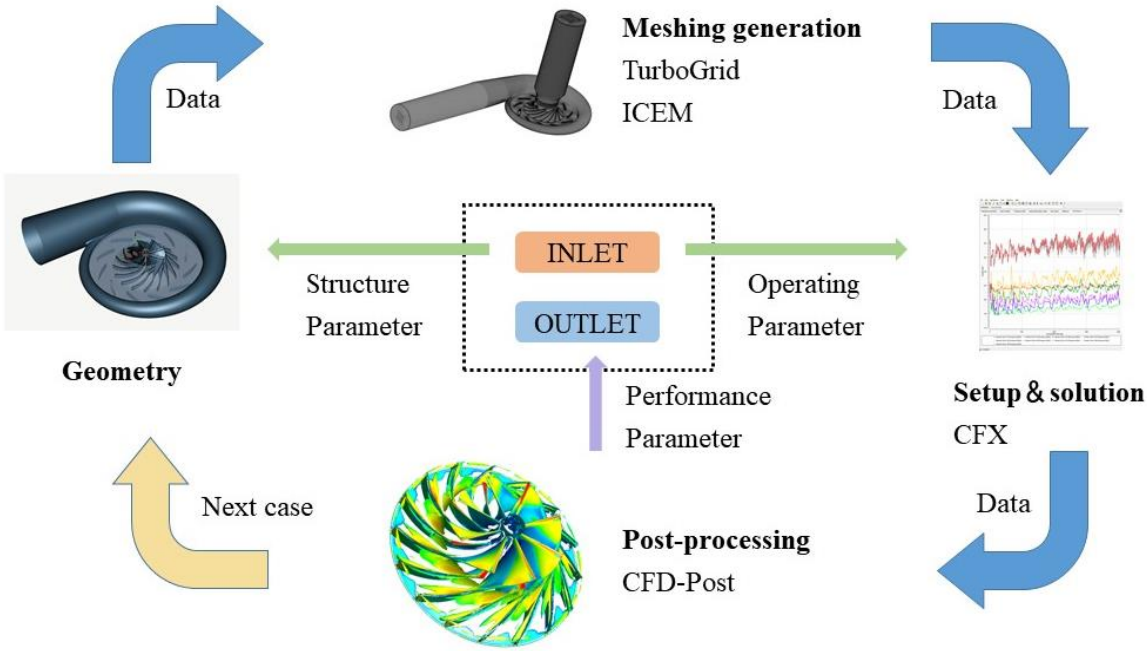

Fig. 5 Schematic of the CFD integrated simulation model for the blower

Figure 4 shows the distribution of Y plus values on the blade and hub of the impeller. The Y plus value represents the dimensionless distance from the first layer of the grid to the wall. On the blade surface, the Y-plus value is less than 3, which satisfies the mesh requirements for the SST turbulence model.

Figure 5 depicts the schematic of the CFD integrated simulation model for the blower. Utilizing the CFD model of the centrifugal blower, a high-fidelity and comprehensive simulation framework is elaborately established. This framework incorporates a series of procedures, including structural parameter input, geometric modeling of the blower, mesh generation, numerical computation, post-processing and data output. The integrated model facilitates seamless data transfer, batch calculation, and automatic data storage among various components, optimizing the simulation workflow to enhance efficiency and accuracy in the analysis of centrifugal blower performance.

3 OPTIMIZATION PROCESS OF BASELINE IMPELLER

3.1 Definition of the Optimization Objectives and Design Variables

The objective of work is to optimize the aerodynamic efficiency of a single-stage high-speed centrifugal blower. The objective is to improve the performance of the centrifugal impeller blades by optimizing their geometric configuration. This will be achieved by increasing the magnitude of variables, the polytropic efficiency (η_{pol}) and the total pressure ratio (P_{tr}).

$$\begin{cases} \max\left(\eta_{pol}\right) \\ \max\left(P_{tr}\right) \end{cases} \tag{9}$$

$$\eta_{pol} = \frac{\dfrac{m}{m-1} RT_1 \left[\left(\dfrac{P_2}{P_1} \right)^{\frac{m-1}{m}} - 1 \right]}{M\omega} \tag{10}$$

$$\frac{m-1}{m} = \frac{\lg \dfrac{T_2}{T_1}}{\lg \dfrac{P_2}{P_1}} \tag{11}$$

where P_1 and P_2 are the inlet static pressures and outlet static pressures, T_1 and T_2 are the inlet temperatures and outlet temperatures, R is the gas constant, M and ω are the impeller torque and angular velocity and m represents the polytropic index, respectively.

In the present study, the camber of the blades at the impeller hub is identified as a key design parameter. The meridian profile of the centrifugal impeller, the number and thickness distribution of the main and splitter blades are maintained in accordance with the baseline impeller.

Bezier curves are continuous and smooth, making them an ideal tool for representing the geometric profiles of blades. Higher-order Bezier curves offer enhanced control over the curve shape and can more accurately capture the intricate variations in blade geometry. By adjusting the control points, the shape of the curve can be modified intuitively. Notably, altering a single control point primarily influences the neighboring segments of the curve while preserving its overall characteristics, thus ensuring local adaptability without compromising the global shape.

The angle between the blade inclination and the meridian plane of the impeller is defined as θ, and the distribution of θ allows for defining the position of the blade on the hub. The distribution of θ for the main blades of the centrifugal impeller on the hub is expressed by a fourth-order Bezier curve with five control points, whose polynomial is shown below:

$$\begin{aligned} \theta(t) = &(1-t)^4 \cdot \theta_0 + 4t(1-t)^3 \cdot \theta_1 \\ &+6t^2(1-t)^2 \cdot \theta_2 + 4t^3(1-t) \cdot \theta_3 + t^4 \cdot \theta_4 \end{aligned} \tag{12}$$

where t is the dimensionless meridional coordinates whose value ranges from 0 to 1, representing from the leading edge of the main blade to the trailing edge of the main blade and θ_0 to θ_4 are designated as the control points on the M-β plane. M is the meridian distance along the shroud and hub contours. θ_0 and θ_4 represent the blade angles at the leading and trailing. The notation M is represented by the following definition (Zhang et al., 2022).

$$M = \int_0^{t_0} \sqrt{\left(\frac{\partial z(t)}{\partial t} \right)^2 + \left(\frac{\partial r(t)}{\partial t} \right)^2} dt \tag{13}$$

where r(t) and z(t) represent the radial and axial coordinates in the meridional plane, respectively. It is a common practice to utilize the radius-normalized meridional distance M', which is characterized as follows (Bourgeois et al. 2010).

$$M' = \int_0^{t_0} \frac{\sqrt{\left(\partial z(t)/\partial t\right)^2 + \left(\partial r(t)/\partial t\right)^2}}{r(t)} dt \tag{14}$$

The blade wrap angle and mounting angle can be converted by the following equation.

$$\theta = \int_0^{c_m} \frac{\tan\beta}{r} \cdot dc_x \tag{15}$$

where θ is blade wrap angle, β is mounting angle, r is current position radius, c is flow length from the inlet side of the blade to the current position and c_m is total length of the flow line (Vavruska et al., 2023), respectively.

The coordinates of the four anchor points for the Bezier curve were selected as the design parameters, with the objective of enhancing the performance of the objective function. The red arrows in Fig. 6 show the possible variations in the position of the Bessel curve

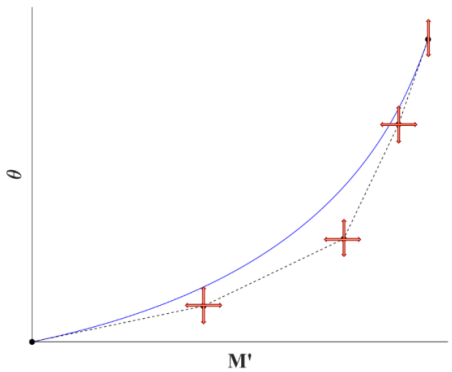

Fig. 6 Definition of the -angle distribution of the centrifugal impeller by Bezier curve

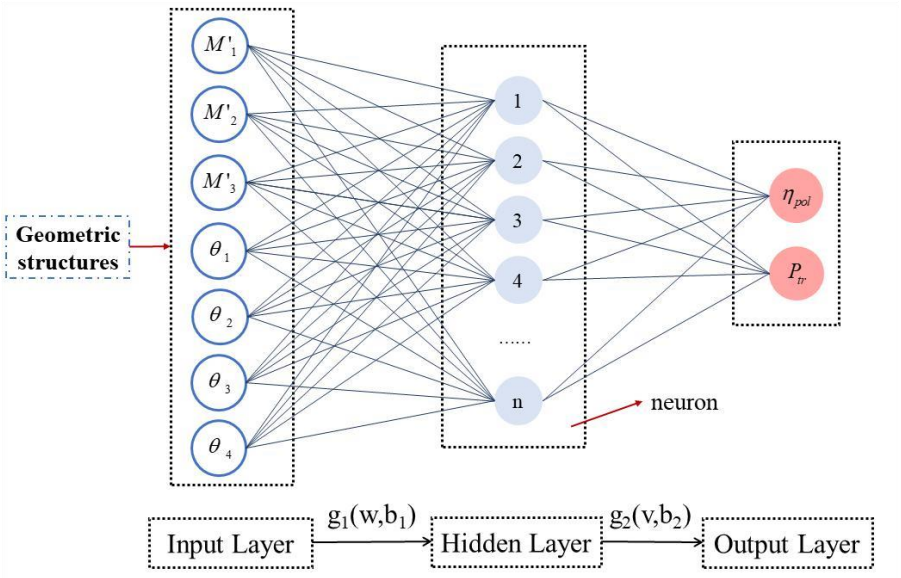

Fig. 7 Topology of BPNN

control points. The θ angle distribution at the top of the blade is well consistent with the baseline geometry for all blades. The θ angle distribution is changed at the root of the blade. In this paper, the blade of the three element impeller is effectively shaped at the leaf root defined by seven design variables.

3.2 Sampling Method for Building Sample Spaces

In this paper, an appropriate sampling technique, namely Latin Hypercube Sampling (LHS), is employed to guarantee the comprehensive representation of the design variables. The fundamental premise is that the range of values associated with each design variable, denote by x_i , is partitioned into n_{LHS} ranges with uniform probability, with a random value chosen from within each segment.

At this juncture, a random and non-replaceable selection is made from one of the n_{LHS} values on x_1 , with each value, each of which is unique. Similarly, on x_2 , a corresponding value is randomly and non-replaceable selected. This pairing process is then repeated for each of the remaining variables within the design, continuing up to a maximum of x_{n_x} (where n_x represents the number of design variables). The aforementioned pairings collectively constitute the initial sample, designated as X_1 . A comparable methodology is employed at each subsequent stage, resulting in a LHS (He & Zheng, 2017).

$$X_k = \left[x_{k1}, x_{k2}, ..., x_{kn}\right], k = 1, 2, ..., n_{LHS} \tag{16}$$

3.3 Approximate Model of Centrifugal Blower Performance Base on SSA-BPNN

The Back Propagation Neural Network (BPNN) employs an error-back propagation algorithm for the purpose of refining the network parameters, with the objective of reducing the discrepancy between the anticipated and actual output values by minimizing the minimizing squared error (Pinapatruni et al., 2024). Figure 5 illustrates the architectural configuration of the BPNN. The structure of the BPNN model comprises three distinct layers: a hidden layer, an input layer, and an output layer. Each neuron is connected through synaptic weights and activation thresholds, represented by w and v , respectively, which signify the weights traversing from the input to the hidden layer and from the hidden to the output layer. Additionally, the value of b represents the activation threshold of the process. The design variables are installed as the input layer, while the polytropic efficiency and total pressure ratio of the blower are severally designated to the output layers of two BPNNs.

The advantage of BPNN is to handle nonlinear problems and have good generalization ability. However, the BPNN also suffers from the problems of being easily trapped in local optimums, being sensitive to the initial weight values, and having a slow training speed.

The Sparrow Swarm Algorithm (SSA) represents a novel intelligent optimization technique inspired by the foraging behavior of sparrow flocks, which is proposed by Xue & Shen (2020). In a manner analogous to the foraging habits of sparrow groups, the SSA assigns the swarm to three specialized roles: predator, follower, and guard. Each of these roles has a unique mechanism for positional updating. The fundamental aspect of the SSA optimization process is the updating of the positions of these three roles: predator, follower, and guard.

The optimization process employs the Levenberg-Marquardt algorithm (trainlm), renowned for its efficiency in minimizing error within neural network contexts. For the hidden layer activation, the hyperbolic tangent sigmoid transfer function (tansig) is utilized, while the output layer leverages the linear transfer function (purelin). To constrain the complexity

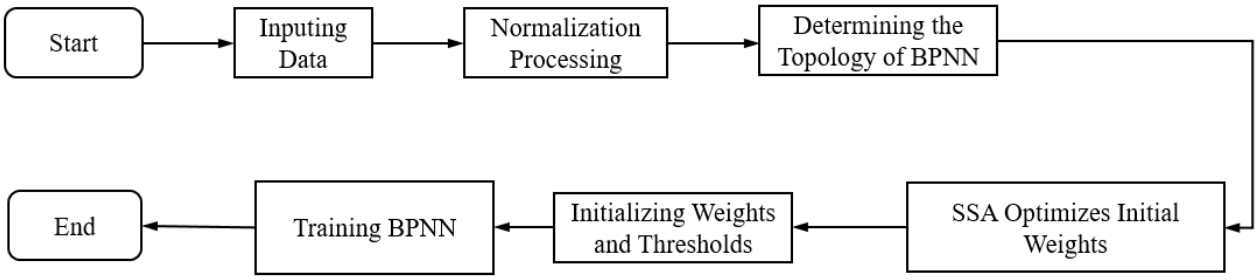

Fig. 8 Process for optimizing BPNN via SSA

Table 3 Details of the SSA for optimizing BPNNs

Criteria	Value
Population size	30
Number of generations	50
Percentage of seeker	0.7
Percentage of guardian	0.2
Percentage of safety value	0.6

and prevent excessive computational demands, the maximum generation count has been capped at 50 iterations.

The process of optimizing the BPNN by SSA is shown in Fig. 8. After the structure of the BPNN topology is established, the weights and bias parameters within the BPNN are utilized as variables in the search space of SSA. Subsequently, the optimal weights and thresholds are calculated through SSA. Finally, the initial weights and thresholds are used to train BPNN to build a proxy model between the centrifugal impeller geometric parameters and the design variables related to blower performance. The total pressure ratio and polytropic efficiency of the centrifugal blower are set as the output layers of two independent BPNNs with hidden layer node counts of 7 and 10, respectively. The accuracy of prediction is separately improved at different performance parameters by the practice of constructing SSA-BPNNs.

Of the 60 pieces of data, 60% were used for training, 20% for validation, and 20% for testing. The selection of trial data was randomized to avoid memory pattern effects (Catrawedarma et al., 2021; Afandi et al., 2022). The fitness function, which amalgamates both the training error and test error, serves to penalize overfitting effectively. This function inherently includes test errors and functions as an implicit regularizer. The global search capability of SSA (presumably a reference to a specific algorithm or methodology) further combats overfitting by investigating a variety of solutions across its search space.

Figure 9 illustrates the detailed configuration of SSA for optimizing BPNNs, where the population size is set to 30 and the number of iterations is limited to 50. Figure 9 presents the prediction results of both the BP and SSA-BP models on the test dataset. Specifically, Fig. 9 (a) and Fig. 9 (c) compare the predicted values of the two models against the sample points, using total pressure ratio and polytropic efficiency as evaluation indicators, respectively. The predicted values from the BP model, depicted by the red line, show significant deviations from the actual values, indicating that the SSA-BP model—configured according to the details in Table 3—achieves a higher level of prediction accuracy. To further validate the precision of the SSA-BP model, the prediction errors of both models are calculated based on the actual values of the sample points. As shown in Fig. 9 (b) and Fig. 9 (d), which correspond to the prediction error values for total pressure ratio and polytropic efficiency, respectively, the SSA-BP prediction errors (represented by the blue line) are closer to zero at most sample points compared to the BP prediction errors (represented by the red line). This demonstrates that the SSA-BP model exhibits smaller prediction errors and superior prediction accuracy.

Figure 10 demonstrates the accuracy of the test data of SSA-BPNNs. The training accuracy of the pressure ratio is depicted in Fig. 10(a), which is a value of 0.98814. Figure 10 (b) illustrates the training accuracy of the polytropic efficiency, which achieves a value of 0.97081. These two neural network architectures have effectively established a correlation between geometric structure and aerodynamic performance. This signifies that these two SSA-BPNNs can effectively establish the connection between impeller structure and blower performance.

3.4 Multi-Objective Optimization Model by NSGA II

The NSGA-II is a widely recognized multi-objective optimization algorithm that is employed extensively across a range of disciplines, including engineering, environmental fields and economics. Its foundation is in the principles of Pareto optimality and non-dominance. The algorithm commences with an initial population, which is then refined progressively in order to identify optimal solutions that balance competing objectives.

$$F\left\{SSA-BP(x_i)\right\}=\left(P_{tr,\max},\eta_{pol,\max}\right);i=1,2,...,7 \quad (17)$$

$$x_{i,\min}\le x_i\le x_{i,\max} \quad (18)$$

where F represents the nonlinear mapping relationship between input and output of a multi-objective optimization model and x_i is design variable whose scope has already been defined at the time of selection, respectively.

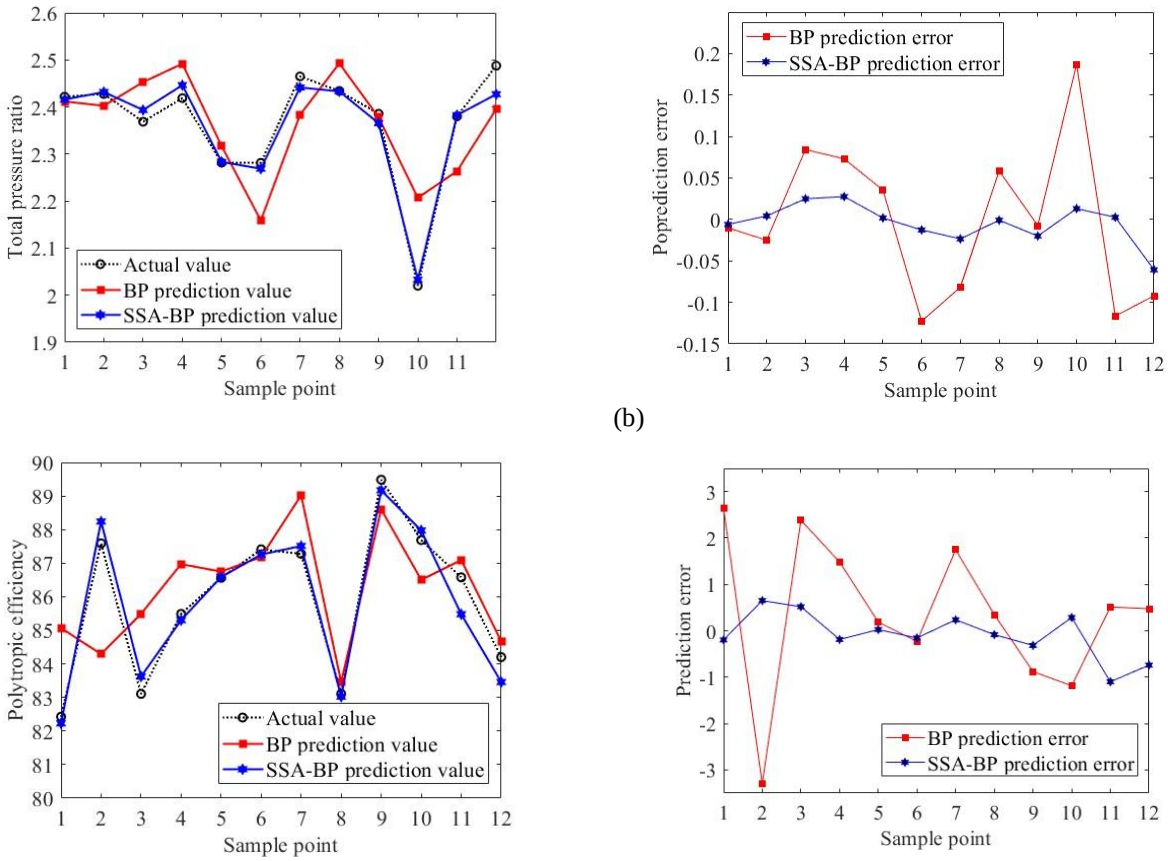

Fig. 9 Prediction results of BP and SSA-BP on test sets

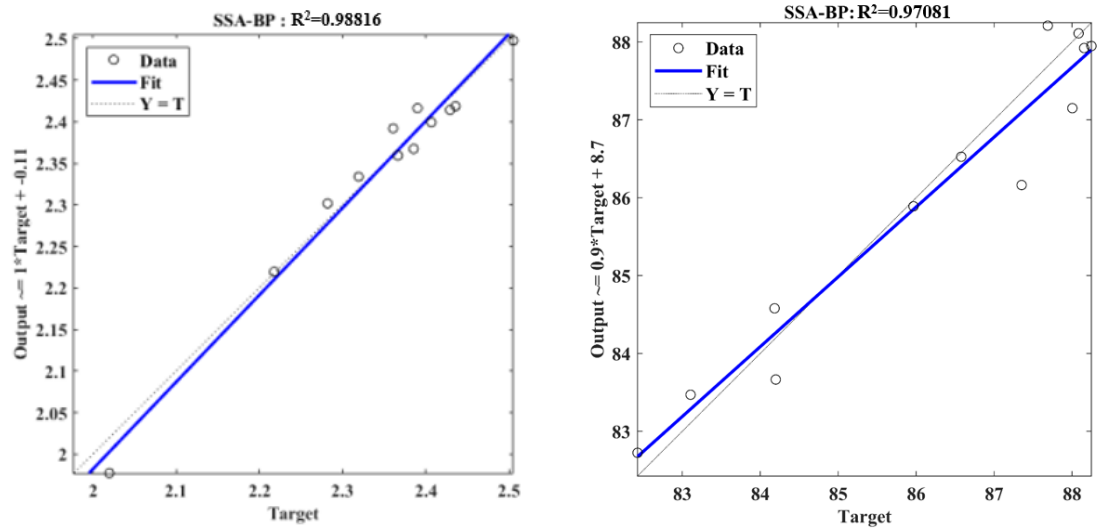

(a)Total pressure ratio (b) Polytropic efficiency

Fig. 10 SSA-BPNNs test data accuracies

The optimization process of multi-objective optimization of the centrifugal blower is shown in detail in Fig. 11. The sampling technique, based on the LHS, is used to obtain the geometric parameters of the centrifugal impeller. The sample library contains 60 sets of new geometric parameters for centrifugal impellers. The CFD techniques are utilized to perform numerical simulations of the sample set. The SSA-BPNN is utilized to train the sample set, and the BPNNs with the best predictive performance are selected as the mapping function. The NSGA-II is employed for optimization until the convergence condition is satisfied.

During the training phase of a BPNN, the quantity of nodes in the hidden layer is initially established, and the

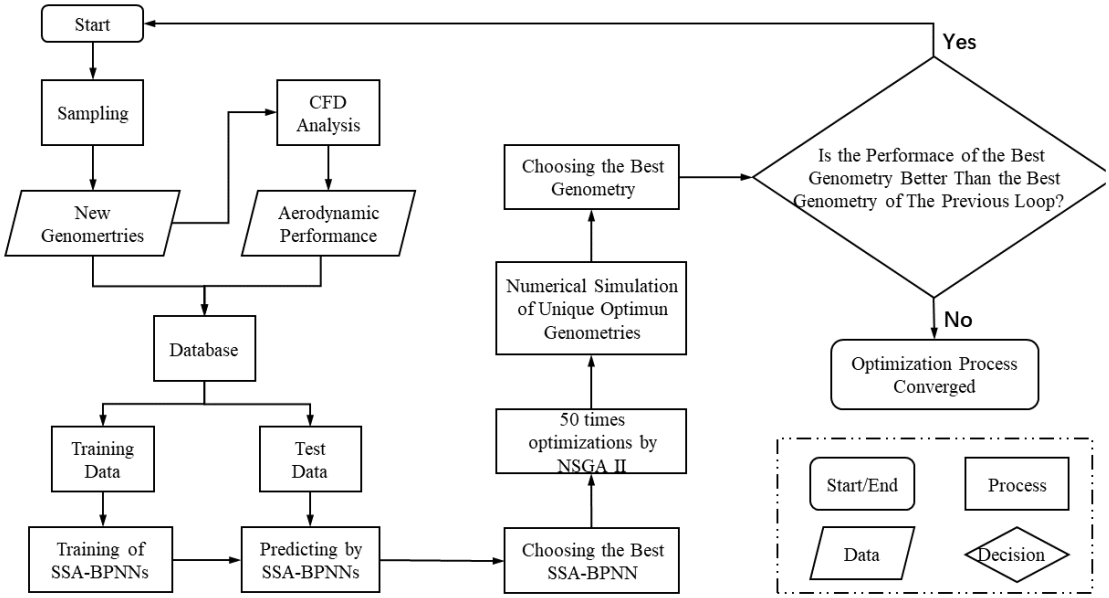

Fig. 11 Process of multi-objective optimization of centrifugal blower

Table 4 Details of the NSGA-II for optimization

Criteria	Function/value
Population size	100
Number of generations	100
Convergence criteria	10^{-4}
Fitness scaling	Rank
Selection	Stochastic uniform
Mutation	0.02
Crossover	0.7

minimum mean square error value of the training set is used as its selection criterion. The total pressure ratio and polytropic efficiency of the centrifugal blower are used as the outputs for training the network structure. The corresponding hidden layer nodes are 7 and 10, respectively. In order to circumvent the propensity of the BP neural network to converge upon a local optimum, the SSA optimization algorithm is implemented in a strategic manner in order to refine the weights and thresholds of the network. The objective of this algorithmic refinement is to enhance the predictive accuracy of the test dataset. Subsequently, the mean square error of the test set as a whole is selected as the fitness value.

Two trained SSA-BPNNs are used as the evaluation function in the NSGA-II to search the optimal of the design space. Table 4 is the details of the NSGA-II for optimization. The graph of the Pareto front is shown in Fig. 12. In the figure, the horizontal coordinate is the polytropic efficiency, and the vertical coordinate is the

total pressure ratio. The optimal solution for the centrifugal blower is a compromise between the maximum polytropic efficiency and the maximum total pressure ratio after several optimization searches, the optimized impeller obtained is represented by the red point in Fig. 12.

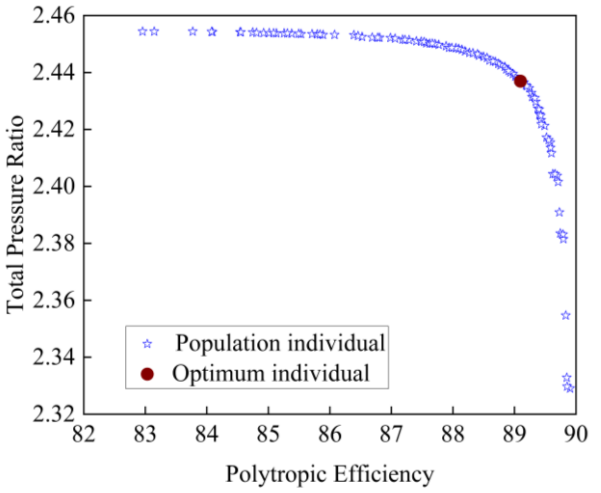

Fig. 12 Pareto front of NSGA II

4 NUMERICAL RESULTS AND DISCUSSIONS

4.1 Result of Optimization

Figure. 13 demonstrates the trend of θ angle at the impeller hub for the baseline impeller and optimum impeller. The control point coordinates corresponding to the optimal individual in the population are extracted and compared with the control point coordinates of the baseline impeller. It is observed that the θ angle at the leading edge of the hub is equal to the baseline in all geometries. In the optimal impeller, the second control point exhibits the greatest horizontal variation, leading to the largest variation in θ values compared to the baseline impeller. At the latter 50% of the Bezier curve, there is little difference appears between the optimal optimum and baseline impellers, but the θ value of the optimal impeller gradually increases towards the trailing edge of the centrifugal impeller. The variation in

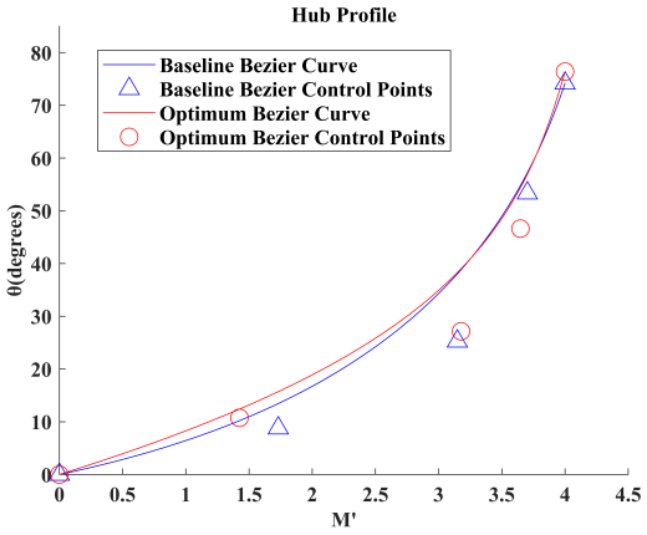

Fig. 13 Comparison of the -angle distribution at hub of the optimum and baseline impellers

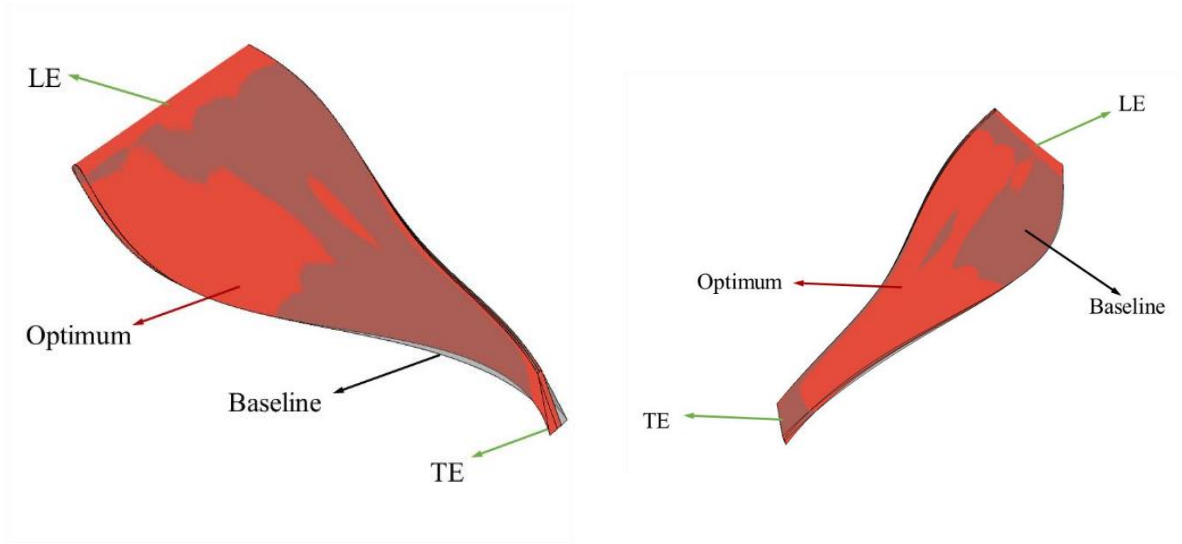

(a) Pressure Side (b) Suction Side

Fig. 14 Geometry comparison of the main blades

Θ values at the root of the centrifugal impeller blades will be reflected in the final blade shape.

Figure 14 represents the comparison of the main blade geometries between the baseline impeller and the optimal impeller. A comparison of the main blade geometry is obtained between the baseline and optimal impellers. Figure 14 (a) is the pressure surface and Fig. 14 (b) is the suction surface. The main blade of the optimal impeller is red and the blade of the baseline impeller is gray. The blade shape of the optimal impeller with the first 50% part of the blade pressure surface at the hub is prominent, which coincides with the trend of θ angle. Meanwhile, at the trailing edge of the blades, the shape of the blade changes from perpendicular to the hub of the baseline blades to tilting towards the pressure surface at the hub due to the increase of the θ angle at the hub.

4.2 Steady Flow Characteristics of the Centrifugal Blower

The results of the numerical calculations of the baseline blower and the optimal blower are compared and analyzed to investigate the effect of structural changes on the internal part of the flow field. To further gain insight into the impact of varying blade configurations on the impeller and centrifugal blower flow, the surfaces at different blade heights (termed 'span') are selected for analysis, with a focus on fluid mechanics and the evolution of flow separation. As shown in Fig. 15, the planes are highlighted with distinct colors at different spans of the impeller and the lines on the blades at different spans. The concise diagram of span profiles is described in Fig. 15 (a) and Fig. 15 (b) is the position of different spans on the blades. The intervals ranging from 0.2 to 0.8 are consecutively allocated as depicted by the arrows in Fig. 15. Figure 16 represents the Mach number distribution of the baseline and optimum impellers at

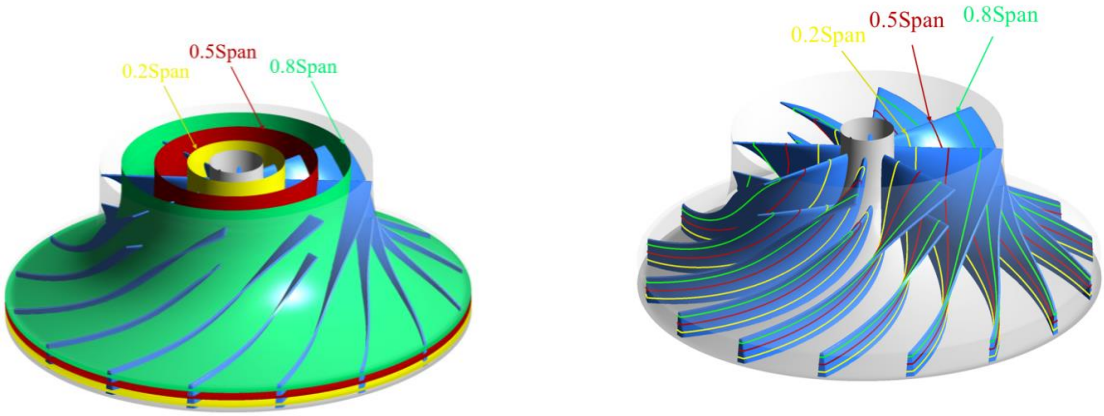

(a) (b)

Fig. 15 Locations of different spans in centrifugal impellers

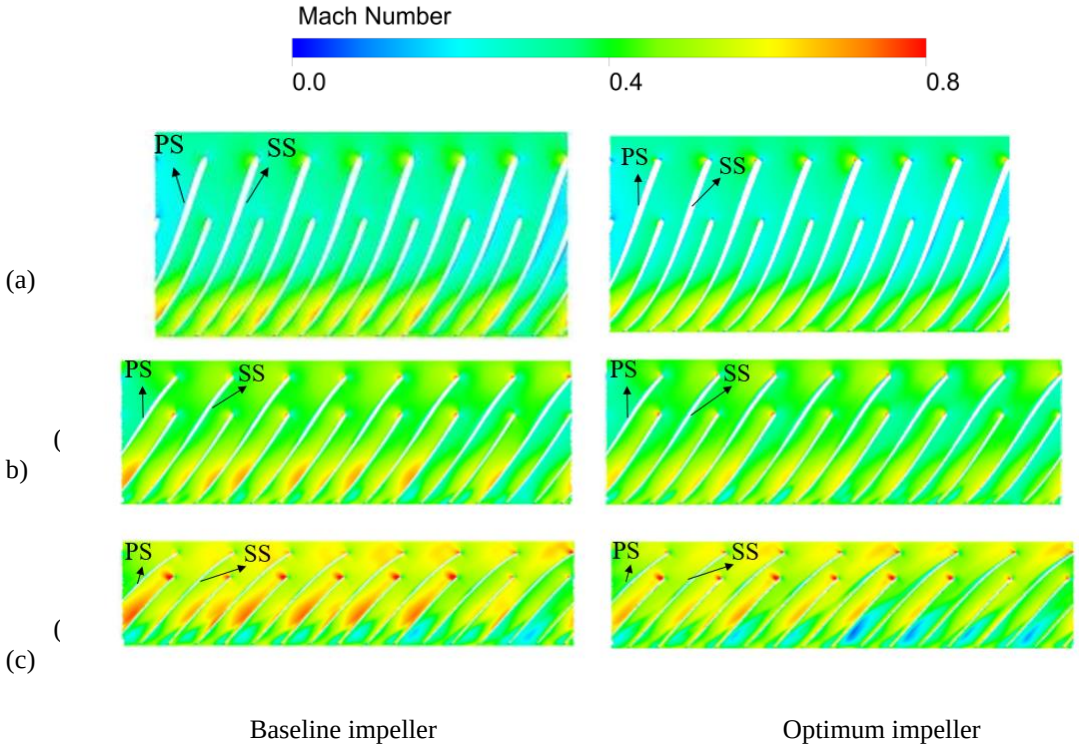

Fig. 16 Comparison of much number on different spans (a) 0.2Span; (b) 0.5Span; (c) 0.8Span

different spans. The distinctive, asymmetric worm-shaped casing structure compromises the integrity of the internal flow patterns, resulting in the impeller rotating in a counterclockwise direction.

The flow mechanism of this centrifugal blower is presented through the Mach number distribution. As illustrated in Fig. 16, we can see that the Mach number distribution within the channels demonstrates that the high Mach number regions are predominantly concentrated along the pressure side (PS) of the blade, while the regions of low Mach number are primarily located near the blade's suction side (Verstraete et al. 2010). The flow architecture in the vicinity of the blade's suction side (SS) is distinguished by a considerable degree of complexity.

Figure 16(a) and Fig. 16(b) show the distribution of Mach numbers at 0.2 span and 0.5 span, respectively. At 0.2span and 0.5span, there is no significant change in the Mach number at the leading edge of the blade and the pressure surface at 0.5 span. The Mach number value gradually decreases and the range of high Mach numbers gradually decreases. A significant decrease in the Mach number appears at the pressure surface of 0.8 span which is shown in Fig. 16(c). At 0.8 span, the area of high Mach numbers at the leading edge of the blade further shrinks. In particular, the flow loss in the impeller is effectively reduced at the leading edge of the splitter blade.

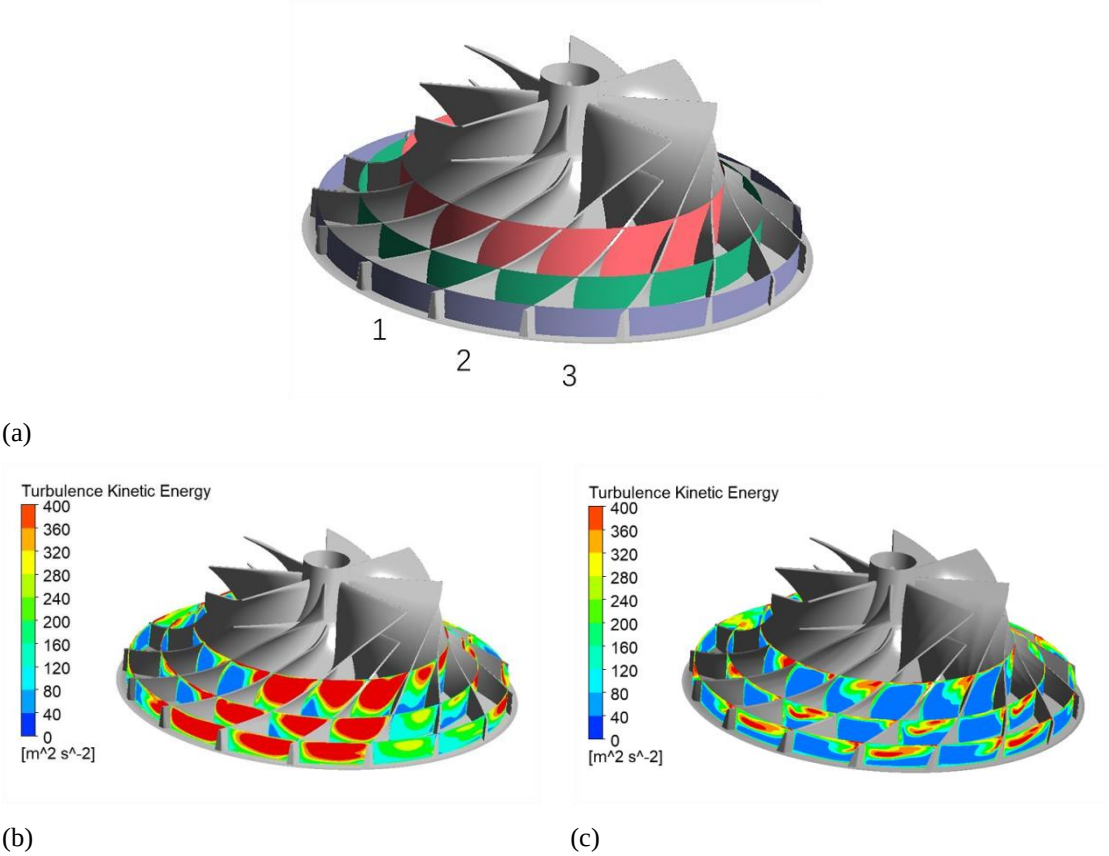

Fig. 17 Circumferential distributions of turbulent kinetic energy along flow passage (a) circumferential cross-section distribution (b)baseline(c)optimum

Figure 17 presents the circumferential cross sections at various radii within the centrifugal impeller channel, along with the circumferential distribution of turbulent kinetic energy across these cross - sections. As shown in Fig. 17 (a), three annular cross-sections with radii of 120 mm, 150 mm, and 180 mm are defined, corresponding to channel 1, channel 2, and channel 3, respectively. The circumferential turbulent kinetic energy distributions in the baseline and optimized impellers are shown in Fig. 17 (b) and Fig. 17 (c), respectively. It is clearly observed that strong turbulent kinetic energy exists in all three flow channels within the baseline impeller in Fig. 17 (b). In these channels, the turbulent kinetic energy is higher in the cross-section closer to the center of rotation and gradually stabilizes along the flow path. The presence of high turbulent kinetic energy regions in the flow channels indicates concentrated energy dissipation, where the vortex core splits into smaller-scale vortices, thereby increasing turbulent friction losses. The high turbulent kinetic energy region in the flow channel of the centrifugal impeller shows that the energy dissipation is concentrated, and the vortex nucleus in the flow channel splits into small scale vortices, which increases the turbulent friction loss. Furthermore, the tip leakage vortex mixes with the main flow, leading to additional energy loss. The tip leakage vortex also generates strong periodic shear forces on the shroud wall, which can accelerate metal fatigue. Suction surface separation vortex leads to local velocity abrupt change, which leads to cavitation incipience risk. In Fig. 17 (c) it can be seen that the regions of strong turbulent kinetic energy are significantly reduced across large areas within the three flow channels of the optimized impeller. A region of strong turbulent kinetic energy still exists close to the pressure surface of the blades and gradually develops along the direction of airflow towards the center of the flow channel. The peak value of turbulent kinetic energy decreases with the decrease of discrete vorticity.

Figure 18 demonstrates the average static pressure distribution of the main blades at different blade spans. The horizontal coordinates are normalized, starting from the trailing edge of the blade suction surface and ending at the trailing edge of the blade pressure surface. The vertical coordinates represent the average values of the static pressure distributions on eight main blades at different spans. Figure 18 (a) and Fig. 18 (b) are the static pressure distributions of the baseline impeller and the optimum impeller at 0.2 Span, 0.5 Span and 0.8 Span, respectively. Dramatic static pressure field variations are found at the leading edge of the blade with high fluctuations in static pressure values. The suction side experiences a larger static pressure gradient, leading to the occurrence of more chaotic static pressure fields and flow separation. With increasing blade height, the variation of static pressure at the leading edge becomes more pronounced due to a decrease in blade thickness and an increase in curvature. The pressure gradually increases along the blade length and some phenomenon is clearly observed. In the baseline impeller, an adverse pressure gradient occurs at 0.8 Span on both the suction

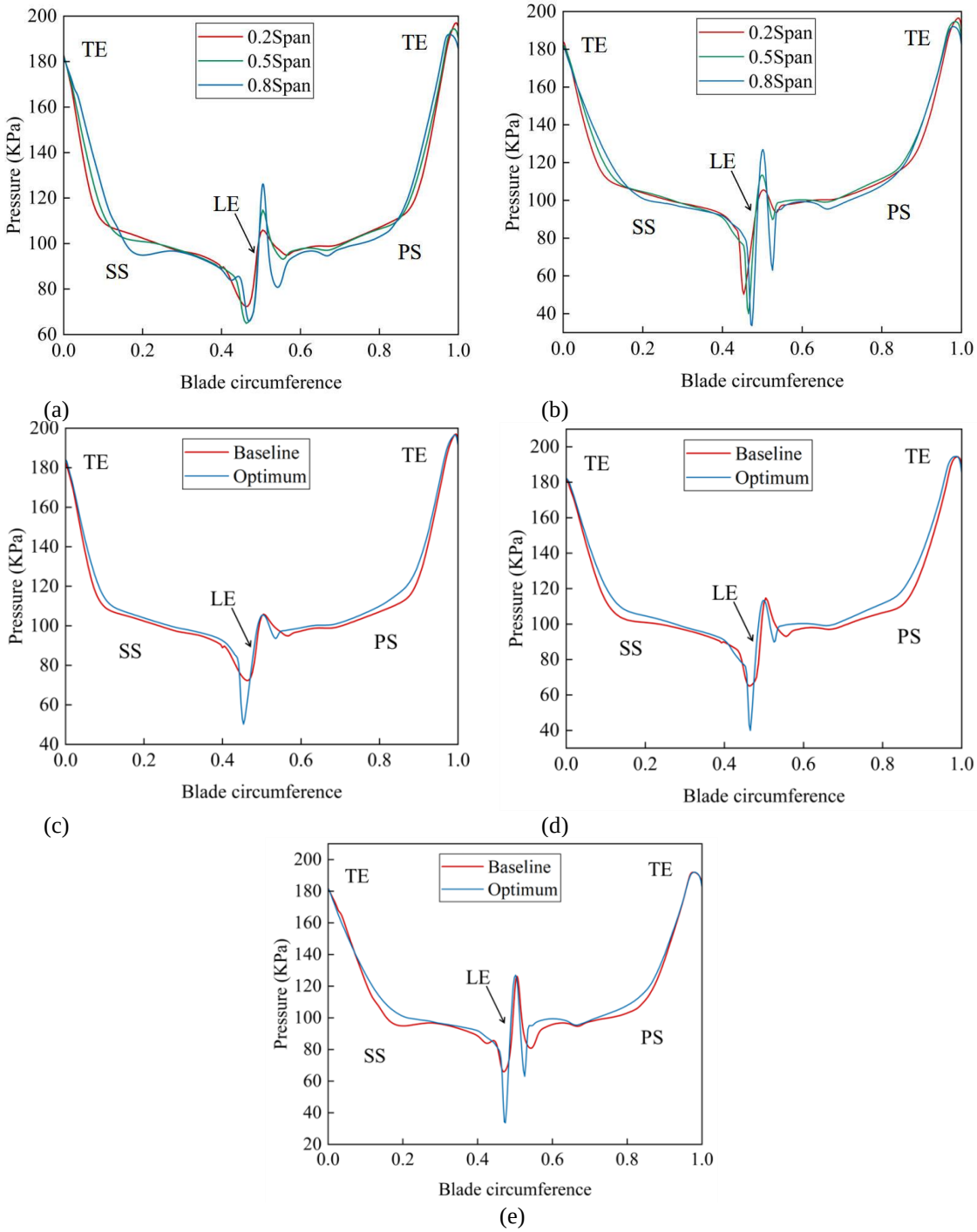

Fig. 18 Static pressure comparison at different spans on main blades of centrifugal impeller (a)baseline; (b)optimum; (c)0.2Span; (d)0.5Span; (e)0.8Span

and pressure surfaces. This phenomenon weakens the boundary layer of the suction surface, leading to separation vortices and potentially inducing secondary flows. In this region, the adverse pressure gradient may superimpose with tip clearance vortices and mainstream bending effects, thereby exacerbating flow separation. In contrast, in the optimal impeller, the adverse pressure gradient on the suction surface is eliminated, while the static pressure gradient on the pressure surface becomes more uniform. The static pressure distribution of the optimal impeller is more uniform at different blade heights, and a higher difference from the baseline impeller occurs at the same position of the blade for different blade heights. At the middle of the blade, the increase of static pressure is more gentle for the optimal impeller and more drastic for the baseline impeller. This indicates that the stability of the optimal impeller is better than that of the baseline impeller.

Figure18(c), Fig. 18 (d) and Fig. 18 (e) are the comparisons of the static pressure distributions between the baseline and optimum impellers at 0.2 Span, 0.5 Span and 0.8 Span, respectively. At specific lobe heights along the pressure surface of blades within the baseline impeller configuration, the hump-shaped fluctuations are evident due to vortex clusters formation which may have destabilizing effects on fluid flow behavior. The sharp

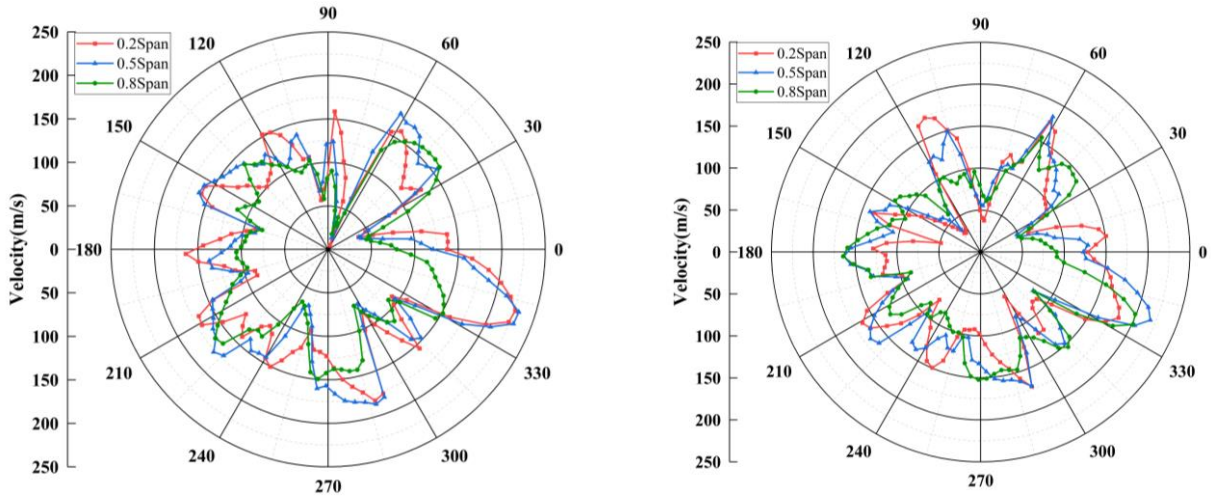

Fig. 19 Comparison of velocity circumferential distribution at different spans of centrifugal impeller outlet

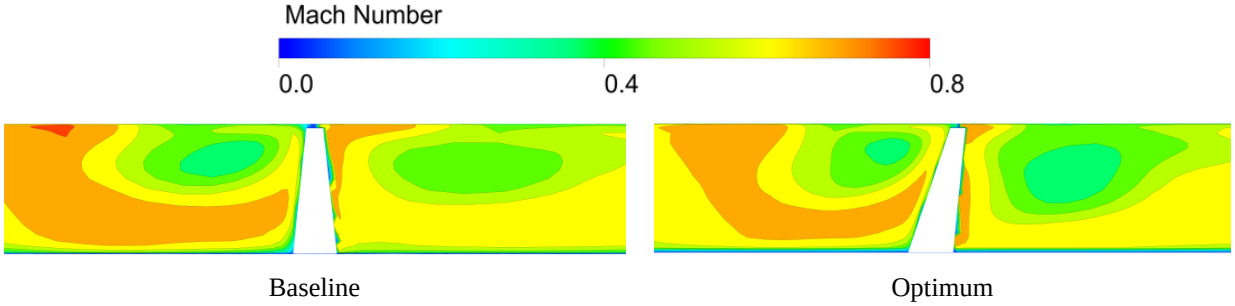

Fig. 20 Comparison of Mach number at outlet of centrifugal impellers

fluctuations of pressure with one positive peak and two negative peaks are prominently captured near leading edges of blades. Positive peaks remain consistent across different lobe heights for both baseline and optimum designs. However, negative peaks exhibit an increasing trend with lobe height particularly noticeable on the suction plane where the difference between these two troughs becomes significantly high.

The circumferential velocities of the baseline impeller and the optimum impeller are shown in Fig. 19 at three different spans, 0.2span, 0.5span and 0.8span. The difference in the velocity distribution at the outlet between the baseline and optimal impellers can be clearly seen in Fig. 19, where the peak velocity of the optimal impeller is smaller than that of the baseline impeller, and the blockage in one of the flow channels of the baseline impeller disappears.

The flow paths on both sides of the same blade are taken into account, and the Mach number distribution is displayed in Fig. 20. The exit Mach number signifies the extent of flow losses at the point where the centrifugal impeller discharges. Considering the same mass flow rate for both types of centrifugal impellers, the average outlet Mach number for the optimized impeller is 0.5774. The average outlet Mach number for the optimized impeller is slightly higher than that of the standard impeller, which is 0.5734. This indicates a slight improvement of the flow uniformity at the outlet of the optimized impeller. The Mach number at the impeller outlet gradually decreases from 1.13139 for the conventional fan to 0.887554 for the optimized fan. The combination of these two features (improved uniformity and reduced absolute Mach number) results in a wider operating range for the optimized blower at the target speed of the centrifugal impeller.

It is also evident in Fig. 20 that the area of the high Mach number region gradually decreases and the Mach number maximum gradually decreases in the flow path at the pressure side of this blade. In the flow path on the suction side of the blade, the area of the high Mach number gradually decreases in the near-wall portion of the blade top, but gradually increases at the blade root.

The formation of vortex structures in centrifugal blowers has a great impact on the flow field and external characteristics. The Q-criteria are introduced to analyze the method that can better reflect the equilibrium relationship between the rotation and deformation of the fluid micro-cluster, and its expression is as follows (Li et al. 2024; Sun et al. 2024a):

$$\Omega_{ij} = \frac{1}{2}\left(\frac{\partial u_i}{\partial x_j} - \frac{\partial u_j}{\partial x_i}\right) \tag{19}$$

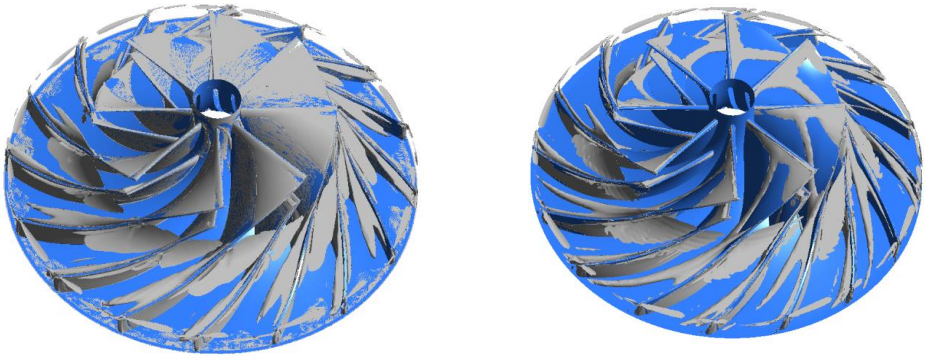

Baseline Optimum

Fig. 21 Comparison of vortex structure inside the centrifugal impeller

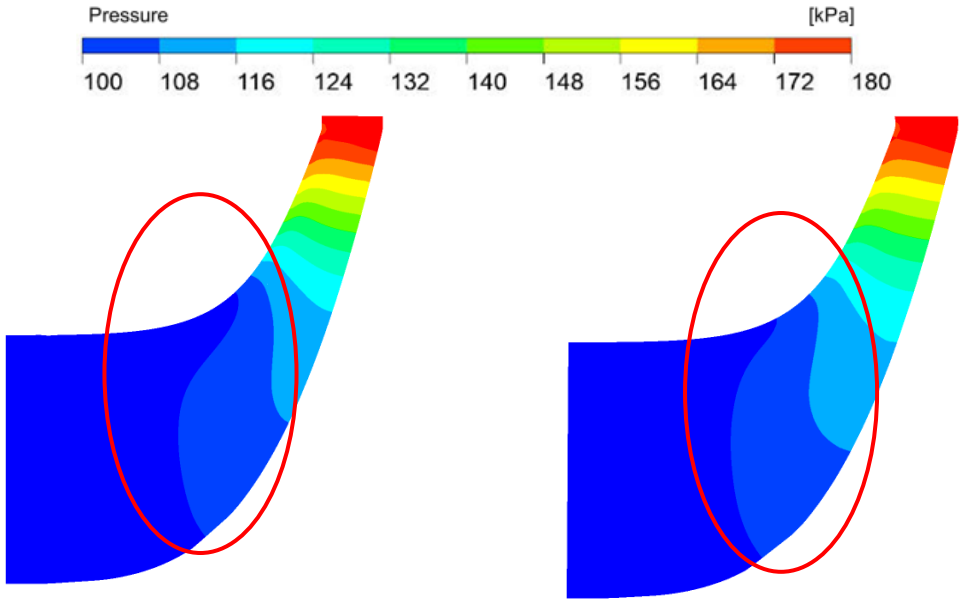

Baseline Optimum

Fig. 22 Comparison of static pressure on meridional plane of centrifugal impeller

$$S_{ij} = \frac{1}{2}\left(\frac{\partial u_i}{\partial x_j} + \frac{\partial u_j}{\partial x_i}\right) \tag{20}$$

$$Q = \frac{1}{2}\left(\|\Omega\|^2 - \|S\|^2\right) \tag{21}$$

where Ω_{ij} represents the antisymmetric part of the velocity gradient tensor and S_{ij} represents the symmetric part, which characterize the rotation and deformation in the flow field.

The physical meaning of the Q criterion is that in the flow field, the vorticity of the rotating part is larger than the deformation and dominates. The values of Q are as follows:

$$Q = \frac{1}{2}\left(\left(\frac{\partial u}{\partial x}\right)^2 + \left(\frac{\partial v}{\partial y}\right)^2 + \left(\frac{\partial w}{\partial z}\right)^2\right) - \frac{\partial u \partial v}{\partial x \partial y} - \frac{\partial u \partial w}{\partial x \partial z} - \frac{\partial v \partial w}{\partial y \partial z} \tag{22}$$

Figure 21 shows the vortex structure at the centrifugal impellers based on the Q criterion (Q = 8.4 × 10^7 [1/S^2]). Within the baseline centrifugal blower impeller, there is a high prevalence of vortex structures, characterized by numerous slender vortex sheets located on the blade surface and in proximity to the hub at both the impeller inlet and outlet. Additionally, a substantial number of striped vortex structures are observed within the region of the impeller tip gap. In the optimal impeller, a large number of fringed vortex structures are observed in the tip clearance region of the impeller. In the optimized impeller design, the decrease of vorticity in the blade suction surface is obviously observed. The volume of the vortex at the high span of the tip leakage vortex and impeller passage also decreases.

Figure 22 demonstrates the comparison of static pressure on the meridional plane of the centrifugal impeller. The region highlighted in red encircles the significant change in static pressure before and after the optimization of the centrifugal blower impeller. In the baseline impeller, the transition change in the low static pressure region of the impeller is more drastic near the

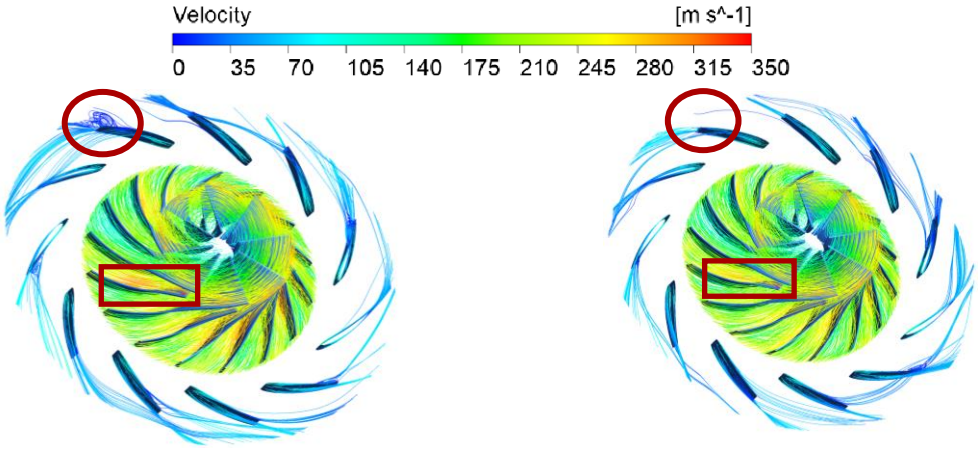

Fig. 23 Comparison of velocity streamlines for impellers and diffusers

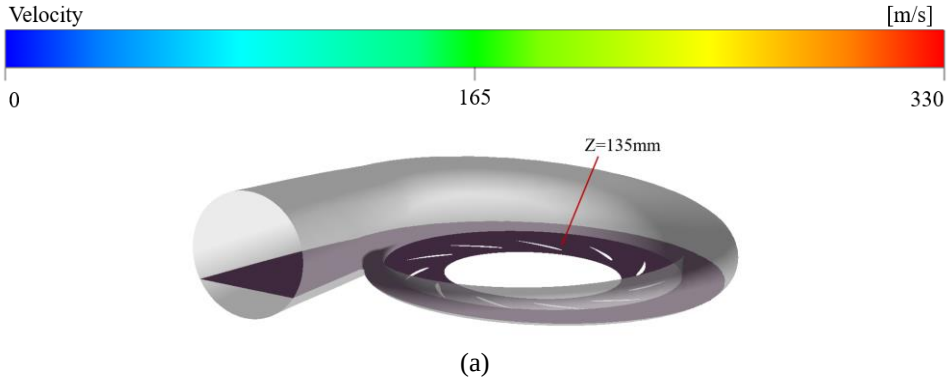

(a)

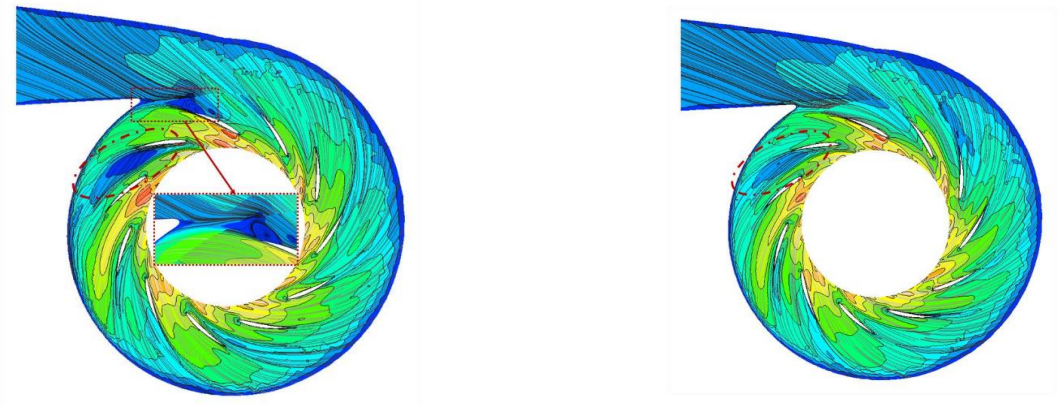

(b) (c)

Fig. 24 Velocity and streamline distribution at circumferential section of diffuser and volute. (a) Circumferential section of diffuser and volute (b) Baseline (c) Optimum

impeller shroud. In the optimal centrifugal impeller, the pressure gradient in this region is more pronounced, indicating that the pressure change of the gas tends to level off as it approaches the shroud. A smaller pressure fluctuation enhances operational safety. The velocity streamlines from the impeller inlet to the outlet are illustrated in Fig. 23. These streamlines effectively indicate the presence of flow blockage within the impeller. Compared to the baseline impeller, the velocity streamlines in the optimized impeller are more uniform. Notably, the baseline impeller displays a wider range of high-velocity zones near its shroud. During operation, distinct separation of vortex clusters (indicated by the red circle) mainly occurs at the trailing edge of the blades in one specific flow path within the vented diffuser, leading to blockage and deterioration of flow inside the impeller. In contrast, for the optimized impeller, this separation vortex disappears, and a reduction in low-speed regions is observed within other flow channels. This indicates that the stability and efficiency of centrifugal blower operation are effectively improved.

Figure 24 presents the velocity and streamline distribution at the circumferential section of the diffuser and volute. Figure 24 (a) indicates the position of the cross-section in the Cartesian coordinate system, with the

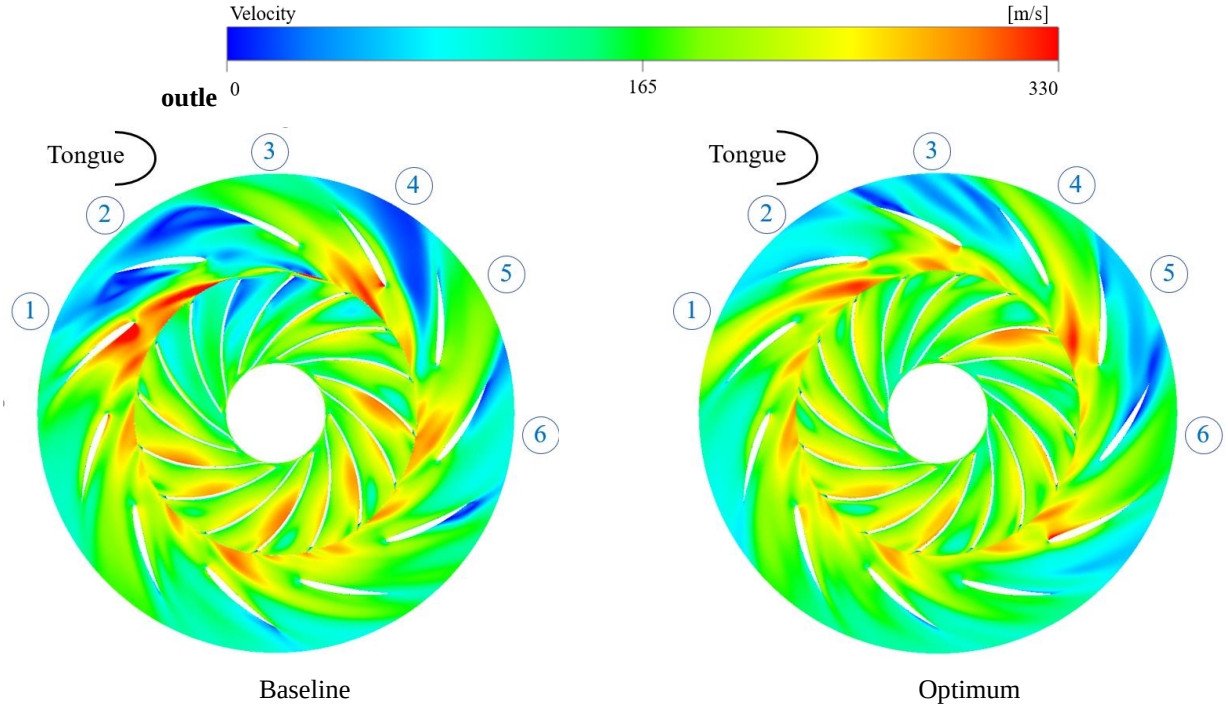

Baseline Optimum

Fig. 25 Comparison of static pressure distribution at half the height of the impeller

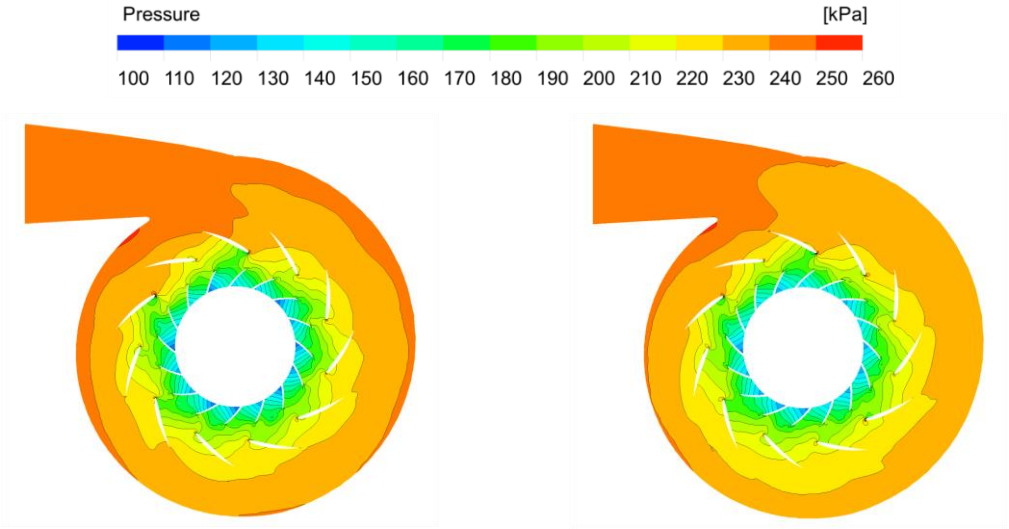

Baseline Optimum

Fig. 26 Comparison of velocity distribution of impeller and diffuser on 0.5Span at 4.6kg/s

section at Z = 135 mm located at 0.5 span of the diffuser. In Fig. 24 (b), flow separation can be seen in the diffuser channel near the tongue. The area enclosed by the red rectangular frame is enlarged to illustrate that a large low-speed region exists at the diffuser outlet due to the influence of the tongue structure, resulting in flow channel blockage. After optimization, as shown in Fig. 24 (c), the backflow vorticity in the tongue region is solved, the area of the low-speed zone shown in the oval red frame is significantly reduced, and the blockage in the flow channel is relieved.

Figure 25 shows the static pressure distribution on the cross-section at half the height of the impeller outlet, including the centrifugal impeller, the diffuser and the volute. In both sections, there is a uniform static pressure distribution inside the impeller and the diffuser, but the pressure is mainly concentrated in the tongue of the baseline volute. In the optimized result, a high-pressure zone still appears, but the pressure concentration is effectively improved, and the area of the high-pressure region is slightly reduced.

Figure 26 shows the velocity distribution of the impeller and diffuser at 0.5 Span under low flow conditions (4.6 kg/s). It can be seen that in the base impeller, there is a low speed zone in the impeller domain, indicating that blockage occurs at this time. In

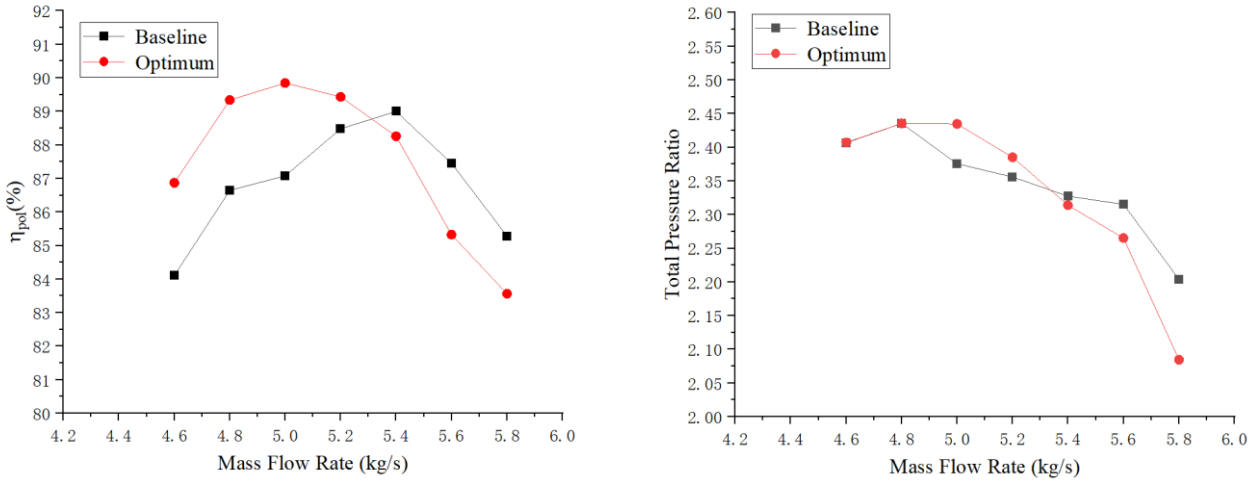

(a) (b)

Fig. 27 Polytropic efficiency and total pressure ratio of baseline and optimum blowers. (a) polytropic efficiency - flow; (b) total pressure ratio-flow

diffuser flow paths No. 1, 2, and 4, there are distinct low-speed vortices at the blade trailing edge and within the flow paths, with evident flow separation. In the optimal impeller, the flow separation on the pressure surface of the impeller outlet blade disappears. In the diffuser, the vortex mass that originally caused the blockage of the flow channel disappeared, but low speed zone appeared in other flow channels (3, 5), and a small number of separation vortices were generated at the trailing edge of the blade.

Figure 27 shows the polytropic efficiency and total pressure ratio between baseline and optimum centrifugal blowers by steady numerical simulations. As depicted in Fig. 27(a), the polytropic efficiencies of both blowers are compared at various mass flow rates. It is can be clearly observed that the polytropic efficiency of the optimized impeller is significantly higher than that of the baseline impeller near the operating flow rates. At the operating mass flow rate, the polytropic efficiency of the baseline blower is about 86.95% while that of the optimized blower is about 89.71%. It is obtained that the polytropic efficiency of the optimum blower is effectively increased by 3.17% compared to the baseline blower. Figure 27(b) shows the total pressure ratio of the centrifugal blower at various mass flow rates. It is further found that the total pressure ratio of the baseline blower is about 2.376, while that of the optimum blower is about 2.435, indicating that the total pressure ratio of the optimized blower is effectively improved by as much as 2.49% at the operating flow rate.

5. CONCLUSIONS

In this paper, the polytropic efficiency and the total pressure ratio of a single-shaft high-flow centrifugal blower are optimized at the operating point by geometric modifications to the centrifugal impeller, while keeping the impeller tip diameter and design speed constant. The optimization process and results of the centrifugal blower are described and demonstrated. The performance and the complex flow characteristics of the high-flow centrifugal blower are thoroughly investigated by numerical simulation. The conclusions obtained are as follows:

A novel approach based on the SSA-BPNN method using Bessel curve control points is proposed to predict the performance of the centrifugal blower. The SSA-BPNN method is employed to predict the geometric parameters and aerodynamic performance of a centrifugal blower for the optimization process.

The steady state flow characteristics of the centrifugal blower are meticulously analyzed through a graphical representation that includes streamlines, static pressure, Mach number and circumferential velocity profiles. Compared to that of baseline centrifugal blowers, the gas velocity uniformity of the optimal impeller is improved across different spans and exits. The pressure gradient is distributed more uniformly within the optimal blower. After optimization, the distribution of the turbulent kinetic energy in the inner circumference of the impeller flow shows a significant decrease in intensity, and the internal flow structure tends to become more stable. The 3D streamline and the Q-criterion accurately describe the structure of the vortex. Compared with the baseline blower, the number of tip leakage vortices and secondary flow vortices in the impeller of the optimal blower is significantly reduced. In the diffuser of the optimal blower, the flow separation phenomenon on the blade surface disappears, particularly at the trailing edge of the blades. The flow separation in the centrifugal impeller and diffuser is effectively suppressed under low-flow conditions.

Furthermore, it is found that the total pressure ratio of the optimized blower increases by as much as 5.98 kPa, corresponding to an improvement of 2.49%. Meanwhile, the polytropic efficiency of the optimum blower reaches approximately 89.71%, representing an increase of 3.18% at the actual operating flow rate.

The significant advancements have been achieved through the successful multi-objective optimization of a single-stage high-flow centrifugal blower in this study, which achieves notable improvements in performance metrics. Following the optimization process, a reduction in gas losses, an attenuation of vortex structures, a decrease in the intensity of turbulent kinetic energy, and an enhancement of flow stability are achieved. These research results can offer data support, establish a theoretical foundation, and provide directional guidance for the performance improvement of centrifugal air blowers. Significant enhancements of total pressure ratio and polytropic efficiency for centrifugal blowers are obtained at the actual operating flow rate, which closely aligns with the overarching objective of energy conservation.

ACKNOWLEDGEMENTS

This work was supported by the National Natural Science Foundation of China (U22A20589), Funds of the National Natural Science Foundation of China (U2006221), Natural Science Foundation Key Projects of Zhejiang Province (LZ22E060002) and Key Research and Development Program of Zhejiang Province (2024C01176).

CONFLICTS OF INTEREST

The authors declare there are no known conflicts of interest associated with this publication and there has been no significant financial support for this work that could have influenced its outcome. We confirm that the paper has been read and approved by all named authors and that there are no other persons who satisfied the criteria for authorship but are not listed.

AUTHORS CONTRIBUTION

C. Lei: Writing-Original Draft Preparation; **J. Zhang:** Methodology, **F. Li:** Investigation; **W. Zhang:** Investigation; **W. Zhang:** Funding acquisition, **Z. Zhu:** Investigation; **Y. Wei:** Writing – Review & Editing.

References

Afandi, A., Lusi, N., Catrawedarma, I. G. N. B., Subono, Rudiyanto, B. (2022). Prediction of temperature in 2 meters temperature probe survey in Blawan geothermal field using artificial neural network (ANN) method. *Case Studies in Thermal Engineering*, *38*, 102309. https://doi.org/https://doi.org/10.1016/j.csite.2022.102309

Arias-Montaño, A., Coello Coello, C. A., & Mezura-Montes, E. (2011). Evolutionary ALGORITHMS applied to multi-objective aerodynamic shape optimization. In S. Koziel & X. S. Yang (Eds.), *Computational Optimization, Methods and Algorithms* (pp. 211-240). Springer Berlin Heidelberg. https://doi.org/10.1007/978-3-642-20859-1_10

Bourgeois, J. A., Martinuzzi, R. J., Savory, E., Zhang, C, & Roberts, D. A. (2010). Assessment of Turbulence Model Predictions for an Aero-Engine Centrifugal Compressor. *Journal of Turbomachinery, 133*(1). https://doi.org/10.1115/1.4001136

Catrawedarma, I. G. N. B., Resnaraditya, F. A., & Deendarlianto, Indarto (2021). Statistical characterization of the flow structure of air-water-solid particles three-phase flow in the airlift pump-bubble generator system. *Flow Measurement and Instrumentation*, *82*, 102062. https://doi.org/https://doi.org/10.1016/j.flowmeasinst.2021.102062

Chen, Z. K., Huang, H. Y., Chen, Q. L., Peng, X. Y., & Feng, J. M. (2023). Novel multidisciplinary design and multi-objective optimization of centrifugal compressor used for hydrogen fuel cells. *International Journal of Hydrogen Energ*, *48*(33), 12444-12460. https://doi.org/10.1016/j.ijhydene.2022.11.312

Colorni, A., Dorigo, M., Maniezzo, V., Varela, F. J., & Bourgine, P. E. (1992). Distributed optimization by ant colonies.

Ekradi, K., & Madadi, A. (2020). Performance improvement of a transonic centrifugal compressor impeller with splitter blade by three-dimensional optimization. *Energy*, *201*, 117582. https://doi.org/https://doi.org/10.1016/j.energy.2020.117582

Fu, J. Q., Wang, H. L., Sun, X. L., Bao, H H, Wang, X, Liu, J. P. (2024). Multi-objective optimization for impeller structure parameters of fuel cell air compressor using linear-based boosting model and reference vector guided evolutionary algorithm. *Applied Energy, 363*. https://doi.org/10.1016/j.apenergy.2024.123057

He, X., & Zheng, X. (2017). Performance improvement of transonic centrifugal compressors by optimization of complex three-dimensional features. *Proceedings of the Institution of Mechanical Engineers, Part G: Journal of Aerospace Engineering*, *231*(14), 2723-2738. https://doi.org/10.1177/0954410016673395

Holland, J. H. (1975). Adaptation In Natural And Artificial Systems.

Ju, Y., Liu, Y., Jiang, W., & Zhang, C. (2021). Aerodynamic analysis and design optimization of a centrifugal compressor impeller considering realistic manufacturing uncertainties. *Aerospace Science and Technology*, *115*, 106787. https://doi.org/https://doi.org/10.1016/j.ast.2021.106787

Ju, Y., Qin, R., Kipouros, T., Parks, G. T., & Zhang, C. (2016). A high-dimensional design optimisation method for centrifugal impellers. *Proceedings of the Institution of Mechanical Engineers, Part A: Journal of Power and Energy, 230*, 272 - 288. https://doi/org/10.1177/0957650915626274

Kennedy, J., & Eberhart, R. (1995). *Particle Swarm optimization.* Icnn95-international Conference on Neural Networks,

Kirkpatrick, S., Gelatt, C. D., & Vecchi, M, P, (1983). Optimization by simulated annealing. *Science*, *220*(4598), 671-680. https://doi.org/doi:10.1126/science.220.4598.671

Li, J., Cheng, J. H., Shi, J. Y., & Huang, F. (2012). *Brief introduction of back propagation (BP) neural network algorithm and its improvement.* Springer Berlin Heidelberg,

Li, X., Zhao, Y., & Liu, Z. (2019). A novel global optimization algorithm and data-mining methods for turbomachinery design. *Structural and Multidisciplinary Optimization*, *60*(2), 581-612. https://doi.org/10.1007/s00158-019-02227-5

Li, Y., Zhang, J., Liu, Z., Shu, Y., Wang, Z., Yang, H., Zhang, W., & Wei, Y. (2024). Spatiotemporal characteristics of rotating stall in a centrifugal compressor with a volute at low-flow rate conditions. P*hysics of Fluids*, *36*(3), 037152. https://doi.org/10.1063/5.0197097

Mengistu, T., & Ghaly, W. (2008). Aerodynamic optimization of turbomachinery blades using evolutionary methods and ANN-based surrogate models. *Optimization and Engineering*, *9*(3), 239-255. https://doi.org/10.1007/s11081-007-9031-1

Menter, F. R. (1994). Two-equation eddy-viscosity turbulence models for engineering applications. *AIAA Journal*, *32*, 1598-1605. https://doi.org/10.2514/3.12149

Nejat, A., Mirzabeygi, P., & Panahi, M. S. (2014). Airfoil shape optimization using improved Multiobjective Territorial Particle Swarm algorithm with the objective of improving stall characteristics. *Structural and Multidisciplinary Optimization*, *49*(6), 953-967. https://doi.org/10.1007/s00158-013-1025-3

Ou, M., Yan, L., Huang, W., & Zhang, T. T. (2019). Design exploration of combinational spike and opposing jet concept in hypersonic flows based on CFD calculation and surrogate model. *Acta Astronautica*, *155*, 287-301. https://doi.org/https://doi.org/10.1016/j.actaastro.2018.12.012

Pinapatruni, G., Duddupudi, M., Dash, S., & Routray, A. (2024). On the investigation of the aerodynamics performance and associated flow physics of the optimized tubercle airfoi. *Physics of Fluids*, *36*, 051907. https://doi.org/10.1063/5.0203519

Roy, D., Samanta, S., & Ghosh, S. (2020). Performance optimization through response surface methodology of an integrated biomass gasification based combined heat and power plant employing solid oxide fuel cell and externally fired gas turbine. *Energy Conversion and Management*, *222*, 113182. https://doi.org/10.1016/j.enconman.2020.113182

Sun, L., Yang, J., Liu, X., Sun, D., & Dong, X. (2024a). Diagnosis of unsteady disturbance characteristics induced by the tip leakage vortex in a compressor based on data-driven modal decomposition methods. P*hysics of Fluids*, *36*(5), 055151. https://doi.org/10.1063/5.0205339

Sun, X. L., Wang, H. L., Fu, J. Q., Xia, Y., & Liu, J. P. (2024b) Many-objective optimization for structural parameters of the fuel cell air compressor based on the Stacking model under multiple operating conditions. *Applied Thermal Engineering*, *245*. https://doi.org/10.1016/j.applthermaleng.2024.122786

Tang, X., Gu, N., Wang, W., Wang, Z., & Peng, R. (2021). Aerodynamic robustness optimization and design exploration of centrifugal compressor impeller under uncertainties. *International Journal of Heat and Mass Transfer*, *180*, 121799. https://doi.org/https://doi.org/10.1016/j.ijheatmasstransfer.2021.121799

Vavruska, P., Kratena, T,. Cech, D., Macalka, A., & Peterka, T. (2023). Determination of impeller blade fillet radius for productive finish milling. *The International Journal of Advanced Manufacturing Technology*, *126*(11), 5541-5554. https://doi.org/10.1007/s00170-023-11483-1

Verstraete, T., Alsalihi, Z., & Van den Braembussche, R. A. (2010). Multidisciplinary Optimization of a Radial Compressor for Microgas Turbine Applications. J*ournal of Turbomachinery*, *132*(3). https://doi.org/10.1115/1.3144162

Wang, Y., Liu, T., Meng, Y., Zhang, D., & Xie, Y. (2022). Integrated optimization for design and operation of turbomachinery in a solar-based Brayton cycle based on deep learning techniques. *Energy*, *252*, 123980. https://doi.org/https://doi.org/10.1016/j.energy.2022.123980

Wang, Z., Wei, Y., & Qian, Y. (2020). A bounce back-immersed boundary-lattice Boltzmann model for curved boundary. *Applied Mathematical Modelling*, *81*, 428-440. https://doi.org/https://doi.org/10.1016/j.apm.2020.01.012

Wang, Z., Zhao, R. C., Zhu, Z. Y., Zhuge, W. L., Zhang, Y. J. (2024). A novel multi-objective optimization scheme of electric turbo compressor system in hydrogen fuel cell for reducing energy consumption and axial thrust. *Energy*, *309*. https://doi.org/10.1016/j.energy.2024.133096

Wei, Y., Zhu, L., Zhang, W., & Wang, Z. (2020). Numerical and experimental investigations on the flow and noise characteristics in a centrifugal fan with step tongue volutes. *Proceedings of the Institution of Mechanical Engineers, Part C: Journal of Mechanical Engineering Science*, *234*(15), 2979-2993. https://doi.org/10.1177/0954406219890920

Xue, J., & Shen, B. (2020). A novel swarm intelligence optimization approach: sparrow search algorithm. *Systems Science & Control Engineering*, *8*(1), 22-34. https://doi.org/10.1080/21642583.2019.1708830

Yang, H., Zhang, W., & Zhu, Z. (2019). Unsteady mixed convection in a square enclosure with an inner cylinder rotating in a bi-directional and time-periodic mode. *International Journal of Heat and Mass Transfer*, *136*, 563-580. https://doi.org/https://doi.org/10.1016/j.ijheatmasstransfer.2019.03.041

Zhang, K., Li, J., Zeng, F., Wang, Q., & Yan, C. (2022). Uncertainty Analysis of parameters in sst turbulence model for shock wave-boundary layer interaction. *Aerospace*, *9*, 55. https://doi.org/10.3390/aerospace9020055

Zhang, T. T., Wang, Z. G., Huang, W., & Yan, L. (2016). Parameterization and optimization of hypersonic-gliding vehicle configurations during conceptual design. *Aerospace Science and Technology*, *58*, 225-234. https://doi.org/https://doi.org/10.1016/j.ast.2016.08.020